Differential Requirement for Dimerization of the Membrane-Binding PH–TH Module of BTK in B cells and T cells

Timothy J. Eisen[1,2,5], Sam Ghaffari-Kashani[1,2], Arthur Weiss[3,4], and John Kuriyan[5,6,†]

[1]Department of Chemistry, University of California, Berkeley, CA, United States

[2]California Institute for Quantitative Biosciences, University of California, Berkeley, CA, United States

[3]Department of Microbiology and Immunology, University of California, San Francisco, CA, United States

[4]Division of Rheumatology, Department of Medicine, University of California, San Francisco, CA, United States

[5]Department of Biochemistry, Vanderbilt University School of Medicine, Nashville, TN, USA

[6]Department of Chemistry, Vanderbilt University, Nashville, TN, USA

[†]To whom correspondence should be addressed: john.kuriyan@vanderbilt.edu

Abstract

Bruton's tyrosine kinase (BTK) functions in many types of immune cells and is a major chemotherapeutic target. BTK is activated at the plasma membrane and can dimerize through its pleckstrin-homology and contiguous tec-homology domains (the PH–TH module). The features that support dimerization of the PH–TH module are unique to BTK among the Tec kinases and appeared relatively recently in evolutionary history. Previous studies suggest that dimerization enhances kinase activity by promoting *trans* autophosphorylation, but whether BTK dimerizes in cells via the PH–TH module, and whether this dimerization controls signaling, is unknown. To address this question, we developed a high-throughput mutagenesis assay for BTK function in B cells and T cells. We measured the fitness costs for thousands of point mutations in the PH–TH module and kinase domain, allowing us to assess whether dimerization of the PH–TH module and BTK kinase activity are necessary for function. In Ramos B cells we find that neither dimerization nor kinase activity is required for BTK signaling. Instead, in Ramos cells, BTK signaling is enhanced by mutations that increase membrane adsorption, even at the cost of reduced PH–TH dimerization. In contrast, in Jurkat T cells, we find that BTK signaling depends on PH–TH dimerization and also on kinase activity. These results provide a framework for understanding why PH–TH dimerization is a more recent evolutionary innovation that is not conserved across the Tec family.

Introduction

One of the remarkable success stories in cancer treatment is the development of the small-molecule kinase inhibitor ibrutinib, which targets the Tec-family kinase BTK. BTK plays a critical role in B-cell receptor signaling and is dysregulated in leukemias (Hendriks et al., 2014). Once activated at the plasma membrane, BTK phosphorylates phospholipase C γ (PLCγ), which generates the second messengers inositol trisphosphate and diacylglycerol, triggering calcium flux and initiating various signaling pathways (Pal Singh et al., 2018). The activation of PLCγ represents a transition from receptor-proximal to cell-wide signaling (Lo et al., 2019), and the activation of BTK is a gatekeeper of this transition.

BTK binds phosphatidyl inositol lipids in the plasma membrane through its pleckstrin-homology and contiguous tec-homology domains (the PH–TH module) (Fukuda et al., 1996; Wang et al., 2015a; Chung et al., 2019). PH domains are phosphoinositide-binding domains that are present in at least ~300 different human proteins (Lenoir et al., 2015). PH domains typically bind to phosphoinositide as monomers and without strong specificity (Lemmon and Ferguson, 2000). The PH domain of BTK binds with highest affinity to phosphatidylinositol (3,4,5)-trisphosphate (PIP_3) (Fukuda et al., 1996), and unusually for PH domains, it can dimerize on membranes (Wang et al., 2015a; Chung et al., 2019). The first evidence for dimerization came from a crystal structure of the BTK PH–TH module, determined by Saraste and colleagues in which dimeric PH–TH molecules were observed in the crystal lattice (Hyvönen and Saraste, 1997) (Figure 1A). This dimeric arrangement, referred to here as the "Saraste dimer", has been observed in all other crystal structures of the BTK PH–TH module that have been determined so far, whether alone or as part of larger constructs (Wang et al., 2015a). The PH–TH dimer in these

structures has an interface composed of two loops: the S1 loop (connecting β strands 3 and 4 in the PH domain; residues 41–51 in human BTK), and the S2 loop (connecting β strands 5 and 6; residues 91–100) (Figure 1A) (Hyvönen and Saraste, 1997). The S1 loop controls lipid specificity in the BTK PH domain (Fukuda et al., 1996), as it does in PH domains from other proteins (Lemmon and Ferguson, 2000).

The Saraste dimerization interface is composed of hydrophobic interactions made by residues presented by the S1 and S2 loops. The residues at the interface include Phe^{44} and Tyr^{42} (presented by the S1 loop) and Ile^{92} and Ile^{95} (presented by the S2 loop). Additional interactions between Leu^{29} and Ile^{9}, presented by the neighboring β strands, also appear important for the interface. Mutations of these residues disrupt dimerization, as inferred from the observation that these mutations decrease BTK autophosphorylation (Wang et al., 2015a). These mutations also increase the concentration-dependent diffusion rate of BTK PH–TH molecules on supported-lipid bilayers, indicative of decreased dimerization (Chung et al., 2019). Long time-scale molecular dynamics simulations show that these mutations induce immediate dissociation of the PH–TH dimer (Wang et al., 2019a).

The ability of the BTK PH–TH module to dimerize on PIP_3-containing membranes is intriguing because dimerization is a common mechanism by which tyrosine kinases are activated (Du and Lovly, 2018). BTK dimerization through other mechanisms can enhance BTK activity. For example, artificial dimerization of a CD16–BTK fusion protein induces a rise in intracellular calcium (Fluckiger et al., 1998). The HIV protein Nef can also induce BTK dimerization through the SH2 and SH3 domains of BTK, resulting in activation (Aryal et al., 2022). These observations suggest that the PIP_3-dependent dimerization of the BTK PH–TH module is a mechanism to couple BTK activity to the levels of PIP_3 in the plasma membrane.

The Tec-family kinases all have PH–TH modules (except for TXK) but the structural elements responsible for dimerization of the BTK PH–TH module are absent or drastically altered in other Tec-family kinases. The S1 loop, a key element of the PH–TH dimer interface in BTK, is shorter in other Tec kinases, and residues that contribute to the hydrophobic core in the BTK dimer are absent. Even for BTK, PH–TH dimers cannot be observed in solution, and seem to form exclusively on membranes. Dimerization of the BTK PH–TH module requires relatively high levels of PIP_3 (~1% of total membrane lipids) to occur at all (Chung et al., 2019). Whether the BTK PH–TH dimer is important for signaling in cells has not clearly been established.

BTK has many functions in different cell types. In the classical view, the Tec kinase ITK is confined to T-cell lineages, and BTK, discovered because of its role in X-linked agammaglobulinemia (Vetrie et al., 1993) is expressed in B cells. But BTK has a wider range of expression, with roles in macrophages (Herbst et al., 2015), CD4 and regulatory T cells (Xia et al., 2020), other myeloid lineages (Weber et al., 2017), and dendritic cells (Taneichi et al., 2008).

That BTK may be playing different roles in different cell types has been highlighted by studies showing that in some cells, BTK is required for signaling but its kinase activity is not (Dhami et al., 2022; Wang et al., 2022; Yuan et al., 2022). In diffuse large B-cell lymphoma (DLBCL), inhibition of BTK kinase activity is an effective treatment, indicating that cancer progression requires kinase-active BTK. Unexpectedly, some ibrutinib-resistance mutations found in patients disrupt BTK kinase activity (Wang et al., 2022). This suggests that there are important non-kinase functions for BTK, perhaps including scaffolding functions and the activation of other kinases that are capable of phosphorylating PLCγ2, such as the Src-family kinase HCK (Dhami et al., 2022). Other studies have shown that the non-kinase functions of

BTK are also important in normal physiology, since kinase-inactive BTK can rescue many aspects of B-cell development in a BTK-knockout mouse (Middendorp et al., 2003).

In this study, we set out to understand how BTK PH–TH dimerization contributes to signaling in lymphocytes, using Ramos B cells and Jurkat T cells as models. We developed high-throughput assays in these cells that report on how mutations affect BTK function, and use these assays to examine residues that modulate PH–TH dimerization. We interpret our results in light of the known structures of the PH–TH module (Hyvönen and Saraste, 1997; Wang et al., 2015a). Unexpectedly, we find that BTK signaling depends on dimerization in the Jurkat but not the Ramos system, and that these differences reflect differential requirements for BTK kinase activity in these two cell types.

Results

A conserved signature for BTK dimerization

To provide an evolutionary context for the unique ability of the BTK PH–TH module to dimerize, we performed a phylogenetic analysis of BTK. We examined the sequences of the S1 and S2 loops, as they were shown previously to be critical for dimerization (Wang et al., 2015a; Chung et al., 2019; Wang et al., 2019a). The S1 loop is conserved among Tec kinases. The loop is expected to be proximal to the plasma membrane, and presents charged residues that tune the affinity of BTK for membrane lipids (Fukuda et al., 1996).

The S2 loop is not predicted to be oriented towards the membrane, and it is present in a longer form only in BTK (Ortutay et al., 2008; Wang et al., 2019a). This loop is 36 residues long in BTK but only 14 residues long in ITK. Only the longer form of the S2 loop can support dimerization of the PH–TH module, because the tip of the extended loop bears hydrophobic

residues (Ile^{92} and Ile^{95}) that are important for dimerization (Wang et al., 2015a). This longer loop and its hydrophobic residues are a signature of BTK PH–TH modules that are potentially capable of dimerization. Indeed, ITK, with a shorter S2 loop, does not dimerize on membranes (Chung et al., 2019).

Within the BTK lineage, spanning the jawed vertebrates, the length of the S2 loop is not conserved, and most of the increased length likely results from an exon insertion (Ortutay et al., 2008). We constructed a BTK gene tree using representative sequences from different vertebrate classes (Figure 1B). This analysis used a multiple-sequence alignment of the full BTK sequence in 366 BTK proteins. The tree was rooted using the lamprey (*Lethenteron camtschaticum*) Tec kinase (the only non-BTK ortholog in the tree), the existence of which indicates that the Tec kinases predate the split between jawless (Agnatha) and jawed vertebrates (Gnathostomes) and thus predate the adaptive immune system (Wu et al., 2012).

We then overlaid the presence or absence of the extended S2-loop signature onto the gene tree (Figure 1B). The result shows that the extended S2-loop signature, characteristic of human BTK and consistent with dimerization, arose after the split between ray-finned fishes (Actinopterygii), which do not have the signature, and lungfish (Dipneusti), which do. BTK proteins in the lobe-finned fishes (Coelacanth) also have the extended S2-loop signature, as do all of the other classes examined (Amphibia, Reptilia, Aves, and Mammalia). The S1 loop, important for phosphoinositide recognition in the membrane, is conserved among all these species. These observations suggest that the original function of the BTK PH–TH module, in organisms that have adaptive immunity, required membrane engagement but not PH–TH dimerization.

High-throughput assays for BTK function in B cells and T cells

To understand how dimerization of the PH–TH module of BTK affects signaling in lymphocytes, we developed a high-throughput mutagenesis assay for BTK function. This assay relies on monitoring the cell-surface expression of CD69, a C-type lectin protein that increases expression in response to several different types of stimulation (Cibrian and Sanchez-Madrid, 2017). We tested whether BTK can increase CD69 expression in Ramos B cells and Jurkat T cells. Ramos cells are a Burkitt's Lymphoma B-cell line, derived from a human male, and these cells therefore contain only one copy of the *BTK* gene (Klein et al., 1975). Unlike many other B-cell lines, the Ramos line does not depend on BTK for cell growth (Yuan et al., 2022). Nevertheless, Ramos cells exhibit BTK-dependent calcium responses (Yuan et al., 2022) and correlated CD69 upregulation (Haselmayer et al., 2019). Jurkat T cells are a T-cell leukemia line derived from a human male (Weiss et al., 1984). Heterologous expression of BTK in Jurkat T cells has also been used previously to study BTK function, again by monitoring calcium responses and CD69 upregulation (Tomlinson et al., 2004; Joseph et al., 2013).

We developed an assay for BTK function by first knocking out the single allele of BTK in Ramos cells using CRISPR/Cas9 (Figure S1A). We then added back human BTK with a lentivirus, using an internal ribosome entry site (IRES) followed by EGFP to monitor lentiviral transduction. To assess stimulation, we monitored CD69 expression using FACS in the presence or absence of the anti-IgM (μ chain) stimulatory antibody.

As expected, removal of BTK from the Ramos cells dampened CD69 responses overall (Figure 2A–B), an effect most clearly seen without stimulation in the knockout, when there is complete absence of basal CD69. In the knockout cells, we observed that re-addition of BTK induces CD69 only in the presence of stimulation, indicating that BTK activity still requires the

endogenous regulatory signals when the protein is added using a lentivirus (Figure 2B). In keeping with previous reports, some CD69 expression is observed in the knockout cells when adding back a control virus, indicating that other signaling molecules or pathways contribute to the B-cell response in these cells (Yuan et al., 2022). Even in wild-type Ramos cells, some CD69 expression is observed without simulation or additional expression of a kinase (Figure 2A), presumably due to the low but detectable amount of phospo-PLCγ2 constitutively present in this line (Kim et al., 2004). This is further underscored by many examples of seeming redundancy in B-cell signaling pathways (Dal Porto et al., 2004).

In Jurkat cells, BTK induces strong CD69 expression in response to stimulation with the T-cell receptor (TCR) crosslinking antibody C305 (Weiss and Stobo, 1984) (Figure 2C–D). These responses are even more apparent when using Jurkat cells in which ITK has been knocked out (Figure 2D). BTK expression also induces a modest but detectable amount of CD69 expression in the absence of stimulation, both in ITK-deficient and wild-type Jurkat cells (Figure 2C–D). Addition of ibrutinib decreased BTK-induced CD69 upregulation in the absence (Figure S1B) and presence (Figure S1C) of stimulation, indicating that BTK activity is required for both the basal and stimulation-induced CD69 upregulation. These observations indicate that BTK can compensate for the signaling deficit induced by ITK loss in Jurkat cells and also that BTK induces higher basal activity.

These observations in Ramos and Jurkat cells were used to construct high-through mutagenesis assays. Lentiviruses were prepared with sequences encoding wild-type BTK or variants, and used to transduce a pool of BTK-deficient Ramos or ITK-deficient Jurkat cells at low multiplicity of infection (Figure S1D). CD69-expressing cells were separated from non-expressers using FACS or magnetic-bead separation (see methods). Both the input population

and the selected population were sequenced, and the resulting counts from each variant in both populations were used to generate fitness scores.

We used mRNA-seq to quantify how much CD69 was induced by different variants of BTK in a high-throughput manner. Most previous high-throughput mutagenesis studies have sequenced genomic DNA (referred to as gDNA) to quantify the relative population of variants (Coyote-Maestas et al., 2021; Subramanian et al., 2021; Hidalgo et al., 2022). But in our experiments, mRNA-seq, used to measure mRNA levels, yielded consistently lower variability between replicates than sequencing gDNA. This is presumably due to both the increased copy numbers of mRNA compared to the gDNA in each cell and the amplification that occurs in the reverse transcription step where cDNA is made from mRNA. During this step, cDNA is produced iteratively in a process that results in linear amplification of the mRNA sequence, which maintains copy numbers more precisely than the exponential PCR amplification of gDNA (Muller et al., 2020). The use of mRNA-seq to count variant levels has two additional advantages: (1) because the reverse-transcription step uses a primer that anneals to the IRES, only mRNAs from the viral construct are sequenced, avoiding any endogenous transcripts. (2) Any changes to mRNA expression level that are not reflected in the DNA copy number can be normalized to the unselected pool. Some mutations lead to changes in apparent DNA copy numbers, for example because they are more difficult to amplify by PCR and thus are underrepresented in the final input library, and for these mutations, both DNA-seq and mRNA-seq yield equivalent copy-number measurements. But other mutations only change mRNA levels while leaving the gDNA levels unperturbed. Nonsense-mediated decay, which degrades mRNAs that have stop codons in the protein-coding sequence (Lykke-Andersen and Jensen, 2015), is an example of a process that affects mRNA but not gDNA levels. We see evidence for nonsense-

mediated decay (either in the Ramos cells or in the lentiviral-packaging HEK293FT cells), as the stop codons are consistently among the least well represented in our unselected libraries compared to the other codons (Figure S1E–F).

mRNA-seq read counts in the CD69-selected libraries were normalized to the unselected pool and to the wild-type sequences to develop a metric for "fitness", according the equation 1:

$$Fitness_i = \log_{10}\left(\frac{SortCount_i}{InputCount_i}\right) - \langle \log_{10}\left(\frac{SortCount_{WT}}{InputCount_{WT}}\right)\rangle$$

(eqn 1.)

Here, $Fitness_i$, $SortCount_i$ and $InputCount_i$ are the fitness score, read counts in the CD69-sorted library, and read counts in the input library for a particular variant *i*, respectively. $SortCount_{WT}$ and $InputCount_{WT}$ are the average read counts for the 20–30 different sequences encoding wild-type proteins included in each library. Fitness values above 0 indicate that a particular variant induces more CD69 expression than wild-type BTK (gain-of-function alleles), while values below zero correspond to variants that show decreased CD69 expression relative to wild-type (loss-of-function alleles). In some positions, we observe that synonymous codon substitutions of the wild-type residue change fitness slightly. This may be attributed to synonymous codon effects on translation rate (Hanson and Coller, 2018), and in our datasets these effects are small.

To determine the optimal concentration of stimulatory antibody with which to measure BTK fitness scores, we performed a concentration-course of stimulatory antibody and analyzed the resulting RNA-seq data. We stimulated ITK-deficient Jurkat cells with 8 concentrations of TCR crosslinking antibody and prepared 16 RNA-seq libraries of mutations in the S1 loop: 8 for the input and 8 for the CD69-sorted populations (Figure S2A). As the stimulant concentration is increased, almost all positions in the library tolerate more variation. This can be observed by the increasing overlap of fitness scores for the mutants and the wild-type proteins (Figure S2B). It

can also be observed by the overall weakening of the deleterious effects for some mutants as the stimulatory antibody concentration is increased (Figure S2C). We performed a similar experiment in the BTK-deficient Ramos cells, stimulating the cells with 4 concentrations of anti-IgM stimulatory antibody. In this experiment, the range of fitness scores also decreases with increasing antibody concentration, as in the Jurkat system. Because of this, the biological-replicate agreement, measured by the Pearson correlation between fitness scores from different samples, decreases with increasing stimulatory antibody concentration (Figure S2D). Overall, these experiments in both the Jurkat and Ramos systems, showed that the best measurements of relative fitness were obtained at the lowest concentrations of stimulatory antibodies. Presumably, high levels of stimulation in both the Ramos and Jurkat cells can bypass the requirement for BTK in CD69 upregulation, leading to increased noise in the data.

To assess our approach, we examined the well-characterized BTK mutation E41K in Ramos cells (Figure 2E). E41K is a gain-of-function mutation in BTK that promotes non-specific membrane binding by the PH–TH domain (Li et al., 1995; Fukuda et al., 1996; Maas et al., 1999). Consistent with this, we observe that the E41K BTK variant significantly increases CD69 expression in Ramos cells (fitness score = 0.22 ± 0.04, Figure 2E). One explanation for the activating effect of the E41K mutation is the removal of a negatively charged residue (Glu^{41}) from the vicinity of the membrane, and its replacement by a positively charged residue (lysine). Recent coarse-grained molecular dynamics simulations of the BTK PH domain support this interpretation (Le Huray et al., 2022). Consistent with this, many substitutions of Glu^{41} confer a fitness advantage, not just the lysine. Not all substitutions confer a fitness advantage, however. Proline distorts the polypeptide backbone, and in our data the mutation E41P (fitness score = –

0.09 ± 0.09) is neutral or slightly loss-of-function. Substitution to aspartate, which is chemically similar to glutamate, is neutral (fitness score = –0.07 ± 0.08).

PH–TH dimerization is dispensable for BTK signaling in Ramos B cells

In order to understand how PH–TH dimerization influences BTK signaling, we generated two libraries of variants in which mutations span the S1 and S2 loops. These libraries were composed of point mutations at every position in these loops, including two codons per residue (except for the methionine and tryptophan residues), two stop codons, and several redundant versions of the wildtype sequence. In total, the S1 library was composed of 443 sequences and the S2 library was composed of 401 sequences. The S1 and S2 regions were chosen because the interpretation of the mutations from these libraries could be anchored on previous studies that characterized the roles of these loops in BTK dimerization (Wang et al., 2015a; Chung et al., 2019; Wang et al., 2019a).

The key hydrophobic sidechains at the Saraste-dimer interface include Tyr^{42}, Phe^{44}, Ile^{92}, and Ile^{95} (Wang et al., 2015a) (Figure 3A). The sidechain of Phe^{44} in one protomer packs against the side chain of the same residue in the other protomer. Three previous studies (Wang et al., 2015a; Chung et al., 2019; Wang et al., 2019a) have used mutations at Tyr^{42} to investigate dimerization in experiments using purified proteins, and consistent with their results, we find that all substitutions to Tyr^{42} are loss-of-function (Figure 3B). To our surprise, however, mutation of other hydrophobic residues at the dimer interface did not lead to loss of function. For example, substitution of Phe^{44} by lysine (fitness score = 0.07 ± 0.04) or arginine (fitness score = 0.08 ± 0.06) increases, rather than decreases, fitness. Similarly, substitutions of Ile^{95} by arginine (fitness score = –0.05 ± 0.06) or proline (fitness score = –0.01 ± 0.04) are both tolerated. The proline in

particular is expected to disrupt the small helix presented by the S2 loop, reconfiguring its reciprocal presentation of hydrophobic sidechains at the interface. Overall, these data indicate that dimerization is not critical for BTK signaling in Ramos B cells.

Ramos-cell signaling does not depend on BTK kinase activity

The role of BTK in some human B-cell lines, and the Ramos line in particular, is unusual. Mutations that disrupt BTK kinase activity fully support BTK-induced calcium flux in Ramos and TMD8 cells (Dhami et al., 2022; Yuan et al., 2022). These results are reminiscent of earlier studies that show that the K430R mutation in the kinase domain of BTK (which alters the interaction of the kinase with ATP and attenuates or abolishes kinase activity (Xu et al., 2000)) reconstitutes most of B-cell development in a *Btk*-knockout mouse (Middendorp et al., 2003). They are also consistent with a growing body of literature that describes non-catalytic roles for BTK in a number of cancers, including DLBCL (Wang et al., 2022). Because the Src, Syk, and Tec families of protein tyrosine kinases can all phosphorylate Plcγ2 in vitro (Kim et al., 2004), it seems that BTK in some contexts may function more as a scaffold than as a kinase, acting to support the proper localization of other kinases.

We wondered whether BTK PH–TH dimerization is only important when BTK kinase activity is important. To study this, we mutated residues that are important for BTK kinase activity, and scored the effects of the mutations using our assay. We targeted the histidine–arginine–aspartate (HRD) motif in BTK (residues 519–521) (Figure S3A). This motif is highly conserved among human tyrosine kinases (present in 90% of sequences), with the aspartate residue in the motif being essentially invariant. Among the vertebrate Tec kinases, the HRD motif is present in 98% of sequences, with the aspartate present in 99%. The aspartate residue in

the HRD motif is located below the terminal phosphate of ATP and the hydroxl group of the substrate tyrosine. It is referred to as the "catalytic base" because it is likely to abstract a proton from the substrate hydroxyl group (Johnson et al., 1996). Mutation of the HRD aspartate abolishes kinase activity in other tyrosine kinases (Deindl et al., 2007). We constructed a library of point mutations at positions including and surrounding the HRD motif, including two codons per residue (except for the methionine and tryptophan residues), two stop codons, and several redundant versions of the wildtype sequence. In total, the library comprised 500 sequences and spanned 12 positions in the BTK kinase domain.

The absolute values of the fitness scores from the HRD library were overall much smaller than for the S1 and S2 loop libraries, and the fitness scores showed more variability (Figure S3B). The decreased magnitude of the scores indicated that the motif exhibits substantial tolerance for substitution, which is unexpected given its central location at the heart of the catalytic center of the kinase domain. Consistent with this notion, His^{519} tolerates substitution by both lysine (fitness score = 0.01 ± 0.01) and isoleucine (fitness score = –0.01 ± 0.01). Strikingly, Asp^{521} in the motif tolerates substitution by phenylalanine (fitness score = 0.00 ± 0.01) and alanine (fitness = –0.01 ± 0.01). Substitution of Asp^{521} is not compatible with kinase activity: indeed, mutation of the orthologous aspartate to alanine in yeast PKA reduces the activity of the kinase to 0.4% of wild-type (Gibbs and Zoller, 1991). The overall insensitivity of CD69 expression levels to mutation in this region indicates that BTK signaling in Ramos cells does not require BTK kinase activity.

Kinase activity is required for BTK to substitute for ITK in T cells

We investigated the HRD-motif library using ITK-deficient Jurkat cells instead of BTK-deficient Ramos cells. In stark contrast to our results from the Ramos system, the fitness scores from these experiments exhibited low variability and strong signals (Figure 4A and Figure S4). Examining the effects of substituting the catalytic base, Asp^{521}, we find that it tolerates no substitutions (Figure 4A). All mutations at this position decrease BTK function to the same extent as a stop codon (X), indicating that the ability of BTK to induce CD69 expression in Jurkat cells depends on BTK catalytic activity. At other positions, even very conservative substitutions lead to substantial fitness loss, even if their effects are not as severe as the stop-codon substitution. For example, Arg^{520} (Figure 4A) exhibits substantial fitness loss when substituted for lysine (fitness score = –0.24 ± 0.03, compared to –0.39 ± 0.01 for the stop codons). Similarly, L518I is also loss-of-function (fitness score = –0.16 ± 0.03). This hypersensitivity of residues across the HRD motif and in surrounding residues (Figure S5A) is consistent with the high conservation of these residues and their critical roles in kinase activity.

We also tested the effects of mutations in another part of the kinase that is critical for activity: the activation loop. The activation loop is a flexible segment of ~20–25 residues within the C-lobe that controls kinase activation (Huse and Kuriyan, 2002). Mutagenizing this region and three flanking residues (positions 538-565, with the variation encoded in 1155 total sequences) showed loss and gain-of-function variants that strongly indicate that BTK kinase activity is required for signaling (Figure S5B). Tyr^{551} corresponds to the site of activating autophosphorylation in the activation loops of most tyrosine kinases. BTK phosphorylation of Tyr^{551} relies on either SYK or LYN in BCR signaling (Baba et al., 2001) and all mutations at this position result in fitness loss (Figure 4B). As expected, glutamate and aspartate fail to mimic a

phosphotyrosine residue. L547P (fitness = 0.44 ± 0.08, Figure 4C) is an unusual case where a proline substitution causes gain-of-function. Ibrutinib recognizes an inactive conformation of the kinase domain (Bender et al., 2017). This residue has been characterized previously as a mutation that confers resistance to ibrutinib (Wang et al., 2019b). The experiments reported here were performed without inhibitors present, and so the fact that we still observe the proline mutation as strongly activating indicates that the presence of a proline at position 547 stabilizes the active conformation of the activation loop, decreasing drug affinity in the process.

We examined the effect of mutations to Tyr^{545}, which is at the equivalent position as Val^{600} in BRAF kinase (Figure 4D). The BRAF kinase domain adopts an inactive conformation that resembles that of BTK. The glutamate residue in BRAF V600E destabilizes the hydrophobic interactions made by Val^{600} in the inactive state (Maloney et al., 2021). In BTK, we find that Tyr^{545} when mutated to almost any charged or hydrophilic residues is activating. By contrast, hydrophobic substitutions of this residue, to phenylalanine (–0.58 ± 0.23), tryptophan (–0.12 ± 0.11), glycine (–0.01 ± 0.08), or valine (0.05 ± 0.13), are neutral or loss of function. These data are consistent with a hydrophobic stabilizing interaction made by Tyr^{545} in a manner similar to that seen in BRAF, as expected from the structures of these two kinase domains. Collectively, the effects of mutations in the HRD motif and the activation loop show that kinase activity is required for BTK to substitute for ITK in Jurkat cells.

BTK requires PH-TH dimerization in Jurkat cells

Given the strong dependence of the ITK-deficient Jurkat cells on BTK kinase activity, we asked whether PH–TH dimerization might be more important for signaling in this context compared to the Ramos cells. We transduced the ITK-deficient Jurkat cells with BTK variants encoded by the

S1 and S2 loop libraries and monitored their ability to increase CD69 expression, as before. Overall, the resulting fitness scores from these two libraries agree well between the Ramos and Jurkat cell lines (Figure 5A and Figures S6A–B), with an R of 0.7 over the 441 fitness scores for each mutation at each position in these loops and a close adherence to the y = x line. This result indicates that most of our observations concerning how different substitutions in the PH–TH module affect BTK signaling do not depend on the model system. In particular, recognition of phosphoinositides by the PH domain is important in both Ramos cells and Jurkat cells.

Closer inspection of these data reveals key differences between the cell lines regarding the importance of PH–TH dimerization. We find that the residues in the PH–TH dimer interface (Figure 3A) tolerate almost no substitutions (Figure 5B). For example, Phe^{44}, the key hydrophobic interface residue, is very sensitive to mutation in Jurkat cells (Figure 5B), unlike in Ramos cells (Figure 3B). In Jurkat cells, it tolerates only substitution by tryptophan (fitness score = –0.01 ± 0.06). By contrast, many substitutions of this residue are tolerated in the Ramos cells. Tyr^{42}, the residue mutated to disrupt dimerization in previous studies (Wang et al., 2015a; Chung et al., 2019) tolerates no substitutions in either cellular context.

The sensitivity of Tyr^{42} to mutation in both cell lines may reflect a role for this residue in the stability of the PH domain, in addition to a role in dimerization. In contrast to Phe^{44}, which makes no intramolecular sidechain contacts, the sidechain of Tyr^{42} packs against that of Ile^{9} and Leu^{29} from the same protomer, and these intramolecular contacts may be important for folding of the PH domain. Two previous studies have used mutations of Tyr^{42} to examine PH–TH dimerization in biochemical assays and chicken DT40 B cells (Wang et al., 2015a; Chung et al., 2019). But the data presented here suggest that mutations to Tyr^{42} destabilize the PH domain,

which would decrease the calcium flux in DT40 cells regardless of whether mutations to Tyr^{42} affect PH–TH dimerization.

To understand more about the relative importance of PH–TH dimerization in the Jurkat and Ramos contexts, we prepared constructs in which we removed the entire S1 or S2 loop regions. In the Jurkat cells, removal of either the S1 or the S2 loops decreased CD69 expression to baseline levels. This supports the observation that both membrane binding and dimerization are required for signaling in this system (Figure 5C). In Ramos cells, the protein without the S1 loop also fails to signal (Figure 5D) and is indistinguishable from the control virus. But BTK without the S2 loop has no signaling deficit in Ramos cells. These data, combined with the saturation-mutagenesis data, support a role for PH–TH dimerization in Jurkat but not in Ramos cells.

Membrane binding through the canonical lipid-binding site is required for signaling

The PH domain of BTK shares a canonical lipid binding site with PH domains from other proteins. Biochemical and biophysical studies of the BTK PH–TH module have revealed another lipid-binding site, the peripheral site, that is occupied when the PH module forms a dimer (Wang et al., 2015a; Chung et al., 2019; Wang et al., 2019a). To examine the sensitivity of these two sites in our assays, we generated two additional saturation-mutagenesis libraries that span the canonical PIP_3-binding site (residues 8–36, 1163 sequences) and the peripheral PIP_3-binding site (residues 52–62, 460 sequences). We used the Jurkat cells to measure fitness scores. As expected, the residues that constitute the canonical lipid binding site are sensitive to mutation (Figures 6A–B and S7A–D). In particular, Lys^{12}, Asn^{24}, Lys^{26}, Arg^{28}, and Lys^{53}, which are important for

recognition of the PIP_3 headgroup (Wang et al., 2015a), tolerate no substitution without a loss in fitness.

The mutagenesis data show that the peripheral lipid binding site in the BTK PH–TH domain is not as critical for CD69 expression, as it tolerates more mutations. Consistent with a previous report (Chung et al., 2019), R49S (fitness score = –0.11 ± 0.02) and K52S (fitness score = –0.28 ± 0.14) both individually disrupt signaling (Figure 6C–D). However, Lys^{52} tolerates arginine (fitness score = –0.02 ± 0.08), asparagine (fitness score = –0.02 ± 0.07), glutamine (fitness score = 0.09 ± 0.1), isoleucine (fitness score = –0.02 ± 0.23), and methionine (fitness score = –0.06 ± 0.15). Another residue at the peripheral site, Lys^{36}, tolerates substitutions to arginine (fitness score = –0.01 ± 0.03), serine (fitness score = –0.04 ± 0.1), and cysteine (fitness score = 0.07 ± 0.1). The tolerance at these sites suggests that PIP_3 is not necessarily bound at the peripheral site during signaling, despite the requirement for dimerization in these cells. Two modest gain-of-function substitutions, S55K (fitness score = 0.1 ± 0.07) and S55R (fitness score = 0.04 ± 0.02), indicate that more positive charge near this lipid site can enhance signaling (Figure 6C–D). These substitutions show that while the canonical lipid binding site is crucial, the peripheral site can contribute to signaling, but is not required.

Context-dependent PH-domain mutations

In examining the fitness landscapes for the S1 and S2 loops in the Ramos and Jurkat cells, we noticed a set of mutations that decrease fitness in Jurkat cells but increase fitness in Ramos cells. Surprisingly, many of these mutations tend to be substitutions to lysine or arginine (Figure 7A). Glu^{41}, Phe^{44}, Glu^{45}, Gly^{47}, and Gly^{50}, all of which are in the S1 loop, exhibit this switching behavior most strongly. By contrast, when the wild-type residue is positively charged (Arg^{46},

Arg^{48}, Arg^{49}), it does not exhibit differential fitness when mutated. Although some other substitutions also exhibit differential fitness (Figure S5), these basic substitutions exhibit the clearest trend.

The differential fitness in the two contexts suggests that in Ramos cells, but not Jurkat cells, BTK activation is enhanced simply by increasing membrane localization through increased positive charge in the PH domain. This idea is supported by the observation that the residues that enhance fitness in the Ramos context when mutated to lysine or arginine are predicted to face toward the plasma membrane, based on structures of the BTK PH–TH module (Figure 7B). One such residue is Glu^{41}, for which the mutation E41K is activating (Fukuda et al., 1996). E45K, like E41K is also strongly activating in Ramos cells. But E45K shows an even greater loss-of-function in the Jurkat cells than E41K, an effect that cannot be explained by previous literature. For this reason, we chose to examine E45K further.

The mutation E45K in the BTK PH–TH module promotes membrane binding

To investigate how these mutations in the S1 loop affect membrane binding, we measured the adsorption of the PH–TH module to membranes using purified components. We prepared supported phospholipid bilayers on glass coverslips with 96% 1,2-dioleoyl-sn-glycero-3-phosphocholine (DOPC) and 4% PIP_3. As a control, we used bilayers containing 4% phosphatidylinositol (4,5)-bisphosphate (PIP_2) instead of PIP_3. We purified three variants of the BTK PH–TH module (residues 1-171): PH–TH^{WT}, PH–TH^{E45K}, and PH–TH^{Y42K}, all tagged with mNeon-Green at the C terminus. Bilayer adsorption was quantified by imaging using total internal reflection fluorescence (TIRF) microscopy, which can be used to discriminate between

protein in solution and on the bilayer, as described previously for the BTK PH–TH module (Nocka et al., 2023) (Figure 8A).

When using low solution concentrations of the PH–TH module (5 pM), and imaging using continuous monitoring and a 20 ms exposure, we observed single PH–TH^{WT} molecules diffusing freely across the bilayer. Quantifying the numbers of proteins adsorbed after a 10-min pre-incubation showed that the mutation PH–TH^{E45K} increases adsorption to PIP_3 bilayers (mean fold change of 1.7 ± 0.24, Figure 8B). PH–TH^{Y42K} decreases adsorption to PIP_3 bilayers (mean fold change of 0.23 ± 0.23). This effect is not due to differences in photobleaching (Figure S8A). Nor is the effect due to differences in diffusion rates, measured by per-frame displacements, which are the same for the three proteins at these low densities (Figure S8B). The increase in adsorption of PH–TH^{E45K} is also not due to differences in being able to detect the spots, as the per-spot intensity of the PH–TH^{E45K} is identical to wild-type (Figure S8C). The PH–TH^{Y42K} mutant shows a slight decrease in per-spot intensity, perhaps because of subtle effects of the mutation on fluorophore maturation.

The PH–TH module of BTK does not bind with high affinity to membranes that contain PIP_2 instead of PIP_3 (Chung et al., 2019) (Figure 8C). Strikingly, mutant PH–TH^{E45K} has significant adsorption to PIP_2 bilayers (mean fold change compared to PH–TH^{WT} = 8.2 ± 0.27). Loss of lipid specificity has been reported for PH–TH^{E41K} (Fukuda et al., 1996), and Glu^{41} is located close to Glu^{45}. It seems that loss of the glutamate at either position increases the sensitivity but decreases the specificity of the PH–TH module for PIP_3, an idea supported by the fitness landscapes of PH–TH^{E41K} and PH–TH^{E45K} in Ramos cells (Figures 3B and S6A). In light of this observation, it is interesting that Glu^{45} is unique to BTK among the human Tec kinases that contain PH–TH domains (Figure S8D). ITK, which is more constitutively membrane-

localized than BTK (Tomlinson et al., 2004), has lost the negative charge at this position. Overall, these data provide a mechanism for the increased fitness that we observe in the Ramos system, because PH–TH^{E45K} enhances BTK adsorption to membranes containing either PIP_2 or PIP_3.

The mutation E45K disrupts dimerization of the BTK PH–TH module

We hypothesized that if PH–TH^{E45K} decreased the ability of the PH–TH module to dimerize, this mutation would decrease fitness in Jurkat cells. We used our reconstitution system to test this hypothesis by comparing different surface densities of the PH–TH module, reasoning that dimerization would only occur when the surface density of the PH–TH module on the bilayer was sufficiently high (Chung et al., 2019). In the cell, BTK is recruited to the plasma membrane by both an increase in plasma-membrane PIP_3 and phosphorylation of adaptor proteins, which bind to BTK using SH2-domain mediated interactions. We approximated this recruitment in our reconstitution system by increasing the solution concentration of the PH–TH module, which increases its surface density. Although this does not reflect the ability of the cell to modulate BTK localization while maintaining a constant total concentration, it is a convenient way to modulate the surface density of the PH–TH module, and dimerization, in our reconstitution system.

We increased the solution concentration of the PH–TH module and used TIRF intensity to measure adsorption, rather than single-molecule counts, as we could not distinguish between individual molecules. Surprisingly, PH–TH^{WT} adsorbs more than PH–TH^{E45K} to PIP_3-containing membranes at high solution concentrations of the PH–TH module (100 pM, Figure 8D or 250 pM, Figure S8E). By contrast, PH–TH^{WT} adsorbs less than PH–TH^{E45K} at low solution

concentrations of the PH–TH module (5 pM, Figure 8B). This concentration-dependent effect is not observed on PIP_2-containing bilayers, where PH–TH^{E45K} always adsorbs more than PH–TH^{WT}, regardless of concentration (Figure 8E). These data are consistent with the mutation E45K decreasing the ability of the PH–TH module to dimerize. At high surface densities, PH–TH^{WT} dimerizes, which increases its dwell time on the bilayer (Chung et al., 2019). But at low surface densities, PH–TH dimerization occurs less, and the dwell time of PH–TH^{WT} is determined by unbinding of the monomer from the bilayer. If the mutation E45K disrupted PH–TH dimerization, PH–TH^{E45K} dwell time would be determined by unbinding of the monomer from the bilayer regardless of surface density, and PH–TH^{E45K} would not adsorb to bilayers to the same extent as PH–TH^{WT} at high surface densities.

To examine the effect of the mutation E45K on PH–TH dimerization further, we turned to fluorescence correlation spectroscopy (FCS). FCS measures fluctuations in the fluorescence intensity as molecules diffuse in and out of a small illumination volume. These data can be used to produce an autocorrelation function, which is in turn used to calculate densities and diffusion rates of the fluorescent molecules. FCS analyses have been used previously to show that PH–TH^{WT} dimerizes (Chung et al., 2019). Consistent with this, the diffusion rate of PH–TH^{WT} adsorbed onto PIP_3-containing bilayers is slowed at high surface densities (Figure 8F). By contrast, PH–TH^{E45K} diffuses rapidly at high surface densities (Figure 8F). At low surface densities, both proteins show similar and rapid diffusion, consistent with the lack of difference in diffusion rates observed using single-molecule TIRF (Figure S8C). These FCS data are consistent with the mutation E45K decreasing PH–TH dimerization.

A kinetic model captures the concentration-dependent adsorption of PH–TH^{E45K}. We used a simple two-step model in which PH–TH first binds PIP_3, then the PH–TH::PIP_3 complex

dimerizes (Figure S8F). A more complex version of this model was developed previously, but given our results concerning peripheral-site usage, we chose not to implement the multistep PIP_3 binding components of the other model (Chung et al., 2019). To model PH–TH^{E45K}, we decreased the monomeric dissociation rate constant (k_{-1}) of the PH–TH::PIP_3 complex and decreased the association rate constant of the dimer (k_2). These rate-constant changes cause PH–TH^{E45K} to exhibit higher surface densities than PH–TH^{WT} when both proteins have low initial concentrations (e.g. 5 pM). At high initial protein concentrations (e.g. 100 pM), these rate-constant changes cause PH–TH^{E45K} to exhibit lower surface densities than PH–TH^{WT} (Figure S8G). Collectively, the experimental results together with the kinetic modeling explain both this mutation's loss-of-function in Jurkat cells (which depend on dimerization) and its gain-of-function in Ramos cells (which do not) (Figure 8G).

Discussion

In this study, we leverage the power of high-throughput mutagenesis to examine the mechanism of BTK in lymphocytes. We develop mutagenesis assays in two cell lines: the Ramos B cell and Jurkat T cell, and compare the role of PH–TH dimerization in both. In Jurkat cells, we find evidence for PH–TH dimerization, with a landscape of mutations in the PH–TH dimer interface that is consistent with predictions from the crystal structure of the Saraste dimer (Hyvönen and Saraste, 1997). But we find no evidence for dimerization in Ramos cells. Instead, lysine and arginine mutations at positions that are predicted to juxtapose the plasma membrane increase BTK fitness. In Ramos cells, the recruitment of a monomeric BTK from the cytoplasm to the plasma membrane is sufficient to induce signaling. These differences in signaling are underscored by the E45K mutation, which increases fitness in Ramos cells but decreases fitness

in Jurkat cells. We find that this mutation enhances adsorption of monomeric PH–TH^{E45K} while decreasing PH–TH dimerization.

The main question that arises from this study is why the two cells differ in their requirements for kinase activity and dimerization. One difference between the cells is the adaptor-molecule components of their respective signaling pathways. SLP76 recruits ITK in T cells, and this recruitment is aided by the Linker for Activated T-cell (LAT) and GRB2-related adaptor protein (GADS). LAT is an integral membrane protein and the three adaptors function in collaboration to recruit the signalosome complex. LAT is not expressed in B cells. Instead, B cells express SLP65, which shares substantial sequence and structural homology with SLP76 but seems to combine the functions of LAT, SLP76, and GADS (Yablonski and Weiss, 2001; Koretzky et al., 2006). If BTK were poorly integrated into the LAT/SLP76/GADS signalosome, perhaps due to weaker affinity between BTK's SH2 domain and binding sites on SLP76 (Su et al., 1999), upstream kinases, such as LCK or ZAP70, might not be able to activate BTK in Jurkat. In this case, dimerization provides an alternative pathway for BTK to activate.

A second important difference between the cell lines is that the Jurkat cell has supraphysiological levels of PIP_3 (Shan et al., 2000; Xu et al., 2002). Because characterization of the dimer on supported-lipid bilayers showed that high levels of PIP_3 are required for dimer formation (Chung et al., 2019), the higher PIP_3 levels in Jurkat may induce BTK dimerization. The possibility that PIP_3 levels change the mechanism of BTK signaling, in addition to the amount, is potentially important for some cancers, such as the 3–22% of DLBCL that have PTEN mutations (Wang et al., 2015b). In the physiological setting, antigens that are displayed at precise spacing drive high levels of B-cell signaling, much higher than examined here, and

induce high levels of PIP_3 in the process. Perhaps dimerization is required during this humoral response as well.

PH dimerization may be a more general phenomenon in B-cell signaling. We used the Dali structure server (Holm, 2022) with the 1BTK model (Hyvönen and Saraste, 1997) to search for structures that might be similar to BTK, and unexpectedly found the protein TAPP1 (PDB: 1EAZ, (Thomas et al., 2001)) as the top hit, after additional structures of BTK and one of TEC. TAPP1 was identified from our search in part because it has an extended loop at the same position as the extended S2 loop BTK, a feature that we could only find in the PH domains of these two proteins. TAPP1 and the related protein TAPP2 function in B-cell signaling downstream of the B-cell receptor and are recruited to the plasma membrane via PIP_2 (Marshall et al., 2002; Landego et al., 2012). These proteins contain two PH domains, at their N and C-termini. The alphafold structures (Jumper et al., 2021) of TAPP1 and TAPP2 resemble the BTK Saraste dimer, with the two PH domains interacting with their membrane-binding loops at a similar position to the S1 loop in BTK.

Collectively, the data presented here show that BTK signals in two states. The first state is a scaffolding state, where kinase activity and dimerization are dispensable, but membrane binding is not. The second state depends both on kinase activity and dimerization for signaling. In light of this model, we find it interesting to consider the domain structure of SLP65 as a combined version of the three T-cell adaptors. SLP65 contains a membrane-binding domain (the LZ motif), phosphotyrosine sites, a proline-rich domain, and an SH2 domain. BTK also contains these domains. This implies that BTK itself is a critical cooperative component of the signalosome complex, an idea supported by studies showing that its catalytic function is in many circumstances secondary. Our evolutionary analysis suggests that the monomeric, kinase

activity-independent state may be the ancestral signaling state of BTK, which presumably continues to support the function of BTK in the ray-finned fishes.

Methods

Cell lines

Jurkat T cells and ITK-deficient Jurkat cells (a kind gift from Wan-Lin Lo) were cultured in 5% fetal bovine serum (FBS) in RPMI media without antibiotics supplemented with 1x glutamax (Thermo Fisher). Ramos RA1 B cells (ATCC) and BTK-deficient Ramos cells were cultured in 10% FBS in RPMI supplemented with 1x glutamax. HEK293FT cells (Thermo Fisher) were cultured in 10% FBS in DMEM supplemented with 1x glutamax. All cells were maintained in a humidified incubator at 37ºC and 5% CO_2.

Generation of BTK-deficient Ramos B cells

BTK-knockout Ramos B cells were generated by Crispr/Cas9 technology. sgRNAs targeting BTK (ordered as a pair with its reverse complement, oligos #336 and #337, Table S1) or a non-targeting control (oligos #340 and #341, Table S1) were cloned into the pU6-(BbsI)_CBh-Cas9-T2A-BFP vector (Addgene Plasmid #64323) as previously described (Chu et al., 2015). 40 µg of plasmid was then electroporated into 10 million Ramos RA1 cells using an electroporator (BioRad Gene Pulser Xcell) with a 0.4 cm cuvette and the following settings: 400 µF, 250 V, 1000 Ω using an exponential-decay pulse. Cells were allowed to recover for three days and then sorted to single cells into a 96-well plate based on blue fluorescent protein (BFP) fluorescence using a Sony SH800 cell sorter and a 100 µm sort chip in culture media supplemented with penicillin/streptomcyin. Clones were grown for ~2 weeks or until the media turned orange, then 200 µL of media was added and cells were grown for an additional week. Clones were then plated up to a 24-well plate in replicate plates, and one of the replicates was used for western-

blot analysis. Clones that were BTK-negative were expanded and frozen, along with some non-targeting controls.

Lentiviral production and titering

To prepare lentivirus, HEK293FT cells were seeded at 250,000 cells/mL in 5 mL in 6-cm dishes in culture media (day 1). The next day (day 2), cells were transfected with a mixture of transfer plasmid (modified from pHIV-EGFP, addgene #21373, 5 µg) and two packaging plasmids (pMDG.2, #12259, 1.25 µg and psPAX2, #12260, 3.75 µg) in 500 µL of opti-mem (Thermo Fisher) using lipofectamine LTX (Thermo Fisher) according to the manufacturer's instructions. The following morning (day 3) cells were re-fed. The following day (day 4) 5 mL of viral supernatant was harvested and stored at 4ºC, and the cells were re-fed. The following day (day 5) an additional 5 mL of viral supernatant was harvested and combined with the previous day's aliquot for a total of 10 mL of viral supernatant. This was then concentrated using Lenti-X concentrator (Takara Bio) according to the manufacturer's instructions, and the pellet from this concentration was resuspended in 1 mL of RPMI + 5% FBS, aliquoted, flash frozen in liquid nitrogen, and stored at –80ºC.

Lentiviruses were titered by thawing an aliquot and adding 0, 5, 10, 20, 40, or 80 µL of virus to 500 µL ITK-deficient Jurkat T cells in a 24 well plate, along with 10 µg/mL polybrene. The following day, cells were centrifuged (300g for 5 min) and resuspended in fresh media, then diluted 2x and plated onto a 96-well plate. Cells were grown for two additional days and then the plate was analyzed for GFP fluorescence using an Attune flow cytometer (Thermo Fisher) equipped with a 96-well plate autosampler. The fraction of GFP positive cells as a function of concentration was fit to the standard binding isotherm to obtain titer values.

Library cloning

Saturation-mutagenesis libraries corresponding to regions of interest in BTK were cloned as follows. An oligo pool targeting the region of interest and containing the human wild-type sequence, additional wild-type sequences with random synonymous-codon substitutions, two codon substitutions for each amino acid (except for methionine and tryptophan), and two stop codons at each position was designed and purchased from Twist Biosciences. This oligo pool was designed to have BsaI cloning sites flanking the insert, and sequences were re-coded using synonymous substitution if they contained BsaI, XmaI, or BamHI sites.

Upon receipt, the pool was amplified using PCR for 15-20 cycles in a 50 µL reaction. The two flanking constant regions of BTK (the left and right sides of the insert, Table S1) were also amplified by PCR using primers that added insert-compatible BsaI sites. The three fragments were then column-purified (Zymo DNA Clean and Concentrator) and ligated in a combined digestion-ligation step first at 37ºC for 2 h and then at 16ºC overnight with 1 µL BsaI-HF, 1 µL T4 DNA ligase, 1x T4 DNA ligation buffer, and 20% polyethylene glycol (New England Biolabs) in a total reaction volume of 50 µL. The next day, the reaction was heat-inactivated at 65ºC for 10 min followed by column purification. The sample was then digested for 1 h at 37ºC using XmaI and BamHI in 1x cutsmart buffer (New England Biolabs). The plasmid backbone (pHIV-EGFP addgene #21373) was digested in a separate 50 µL reaction. The sample insert and backbone were then gel purified on a 1% agarose gel.

Following gel extraction and purification using a gel-extraction kit (Qiagen), insert and vector were ligated for 1 h at room temperature in a 20 µL reaction containing 1x T4 DNA ligase buffer and 1 µL T4 DNA ligase, along with a no-insert control. Ligation reactions were column-

purified (Zymo DNA Clean and Concentrator) and eluted in 6 µL. 3 µL of this reaction was used to electroporate Endura electrocompetent cells (Biosearch technologies) according to the manufacturer's instructions, slightly modified as follows. Immediately after electroporation, cells were resuspended in 1 mL of recovery buffer (Biosearch technologies) and grown for 1 h at 30ºC while shaking. This volume was then diluted to 50 mL, and 50 µL were plated onto LB-agar plates containing ampicillin (100 µg/mL). The remaining volume was grown overnight at 30ºC.

The next day, the plates were examined. The experiment was only continued if the library coverage was at least 500x (for example, a 500-variant library needs 250,000 total transformants, or 250 colonies on the sample plate, with little background on the control plate). If the transformation was successful, plasmid DNA was extracted from the 50 mL cultures using a midiprep kit (Qiagen) according to the manufacturer's instructions, and used to prepare lentivirus.

Cell analysis and selection

To measure BTK-dependent CD69 expression using BTK-variant libraries, ITK-deficient Jurkat T cells or BTK-deficient Ramos B cells were plated in 10 mL at a density of 500,000 cells/mL in 10 cm dishes in triplicates or quadruplicates. The cells were then transduced on day 1 with titered lentiviral libraries, adding a volume of virus such that at most 25% of the cells were GFP positive (corresponding to < 3% of cells having a multiplicity of infection > 1) and 10 µg/mL polybrene.

The following morning (day 2) cells were re-fed by centrifugation at 300g for 5 min followed by resuspension in fresh media, with a 2x dilution, and re-plated. Cells were allowed to

recover for one additional day (day 3). On day 4, Ramos cells were stimulated in the evening with 4 μg/mL anti-IgM (I2386, Sigma-Aldrich).

On day 5, Ramos or Jurkat cells were stained with anti-CD69 as follows. Cells were concentrated by centrifugation at 300g for 5 min, then resuspended in 200 μL of cell-staining buffer (phosphate-buffered saline containing 10% FBS and 0.05% w/v sodium azide) containing a 1:20 dilution of PerCP-Cy5.5 conjugated anti-CD69 (Cell Signaling Technology #28633). Cells were then incubated on ice for 30 min in the dark. Following this incubation, cells were centrifuged again and washed with 500 μL cell-staining buffer, then centrifuged and resuspended in 1 mL of cell-staining buffer for sorting. After this staining protocol, 100 μL (10%) of sample was removed as input and kept on ice during sorting. Cells were sorted for a GFP-positive and CD69-positive population on a Sony SH800 Cell Sorter, gating based on single and double negative controls, sorting at least 200x the number of cells as variants in the library.

Following sorting, input and sorted samples were mixed with 1 mL of TRI reagent (Sigma-Aldrich), concentrating the sorted sample by centrifugation (300g, 5 min) if the volume exceeded 200 μL. RNA was extracted according to the manufacturer's protocol, except that after the aqueous phase was transferred to a new tube, it was mixed 1:1 with chloroform and centrifuged at 21,000g for 10 min at 4ºC as an additional wash step. 4 μL of linear acrylamide (Thermo Fisher) was added as carrier.

For some experiments, cell sorting was not required but the fractions of CD69 and GFP positive cells were still analyzed. For these experiments, the Attune flow cytometer was used instead of the Sony SH800, and the protocol for staining cells was exactly above, with one modification. Because of the different laser and filter configurations on the sort instruments, the

staining antibody used for analysis was APC-conjugated anti-CD69 from Biolegend, #310910, which is the same clone as the other conjugate (Cell Signaling Technology #28633).

In experiments using the HRD-motif libraries, CD69-positive cells were separated with a MACS kit instead of a cell sorter, using the CD69 microbread kit II for human (Miltenyi Biotec), according to the manufacturer's instructions.

Library preparation and sequencing

RNA-seq libraries were prepared from TRI reagent-extracted samples as follows, beginning with the reverse-transcription. Following precipitation, RNA was resuspended in water containing 5 µM RT primer (oligo #296, Table S1). The mixture was heated to 65ºC for 5 min, then snap cooled on ice. The RNA–oligo mixture was then mixed with 1x first-strand buffer (Thermo Fisher), 0.5 mM deoxynucleotide triphosphates, 10 mM DTT, 1 µL SuperaseIn (Thermo Fisher), and 0.5 µL Superscript III (Thermo Fisher). The final reaction mixture was incubated at 50ºC for 1 h. Followed this incubation, RNA was hydrolyzed by addition of 5 µL of 1 M NaOH and incubation at 90ºC for 10 min. The mixture was then neutralized with 25 µL of 1 M HEPES, pH 7.4, and desalted using a Micro Bio-Spin P-30 column, in tris (BioRad), eluting the cDNA in 60 µL.

The cDNA was PCR amplified in one round (the S1 loop, S2 loop, and activation loop libraries) or two rounds (the HRD-motif library and the peripheral and canonical-site libraries). In the one-round protocol, long primers that were specific to the template but also added the Illumina adapters, flow-cell hybridizing sequences, and barcodes were used (oligos #209, #210, #211, #212, #213, #214, #215, #216, #217, #218, #219, #220, #221, #222, #223, #224, and #225, Table S1). In the two-round protocol, the first-round PCR added the priming regions for Illumina

sequencing but did not add the barcodes (using primers #323, #324, #328, #329, #391, and #392, Table S1). The second-round PCR used primers that annealed to the Illumina priming regions, adding the flow-cell hybridizing sequences and barcodes (using primers BC_p5_1, BC_p5_2, BC_p5_3, BC_p5_4, BC_p5_5, BC_p5_6, BC_p5_7, BC_p5_8, BC_p7_1, BC_p7_2, BC_p7_3, BC_p7_4, BC_p7_5, BC_p7_6, BC_p7_7, BC_p7_8, BC_p7_9, BC_p7_10, BC_p7_11, and BC_p7_12, Table S1). Amplified libraries were gel-purified on a 2% agarose gel, extracted with a gel-extraction kit (Qiagen), pooled at equal molar based on the band intensities, and then concentrated using a clean and concentrator kit (Zymo). Libraries were sequenced using a MiSeq sequencer and V2 chemistry with paired-end 150 by 150 base reads.

Data analysis

Fastq files from MiSeq runs were aligned to the Fasta files containing the full sequences of each variant using Kallisto (Bray et al., 2016) to generate read counts for each variant. The next steps of data processing proceeded independently for each pair of input and sorted datasets. To generate fitness scores, a read cutoff of 50 reads was first applied to the input libraries such that any variant not passing this threshold was discarded. Next, the unnormalized scores were calculated by dividing the number of reads in the sorted dataset by the number of reads in the input dataset and taking the $\log_{10}$. These unnormalized scores were normalized by subtracting the mean of the wild-type fitness scores, according the equation 1:

$$Fitness_i = \log_{10}\left(\frac{SortCount_i}{InputCount_i}\right) - \langle \log_{10}\left(\frac{SortCount_{WT}}{InputCount_{WT}}\right)\rangle$$

(eqn 1.)

In equation 1, $Fitness_i$ denotes the fitness score for a particular variant i.

The number of wild-type sequences was 20–30, based on the number of positions in the library: because two codons were included for each amino acid that has at least two codons, the number of wild-type variants was the sum of the number of positions and additional sequences with multiple random synonymous substitutions. The fitness scores are plotted ± standard error.

Code to generate saturation-mutagenesis sequences and to analyze RNA-seq libraries was written using R (R Development Core Team, 2022) and Python and is available on Github (https://github.com/timeisen/MutagenesisPlotCode).

Bacterial Expression and Purification of PH–TH modules

The BTK PH–TH module and variants were cloned by ordering a version of the BTK coding sequence (residues 1–171) codon optimized for *E. coli* using the codon-optimization tool (Integrated DNA Technologies). This sequence was PCR amplified (oligos #246 and #421, Table S1) and cloned into the pET-SUMO vector, as described previously (Wang et al., 2015a). The E45K and Y45K mutations were introduced into the PH–TH module by overlap-extension PCR (oligos #414 and #420, Tabls S1). The final construct contained an N-terminal hexahistidine tag followed by a SUMO tag, then the PH–TH module, and a C-terminal mNeonGreen, under the control of a T7 promoter.

The final plasmid was transformed into BL21-DE3 *E. coli* and plated onto kanamycin-resistant plates. Colonies were used to start a 50 mL liquid culture which was grown overnight at 37ºC in terrific broth (TB) containing 50 µg/mL kanamycin. The following morning, 1 mL of the saturated culture was used to start a 1 L culture (TB and 50 µg/mL kanamycin), which was grown until it reached an OD_{600} of 1.5. At this point, protein production was induced by diluting the culture 2-fold with TB containing 50 µg/mL kanamycin, 2 mM Isopropyl ß-D-1-

thiogalactopyranoside (IPTG) and 200 μM $ZnCl_2$, pre-cooled to 4ºC. The 2 L culture was then grown overnight at 18ºC.

The next morning, the bacterial were pelleted by centrifuging at 4000 rpm for 15 min at 4ºC in a swinging-bucket centrifuge. The pellet was resuspended in 10 mL of lysis buffer (20 mM tris, pH 8.5, 500 mM NaCl, 20 mM imidazole, and 5% glycerol supplemented with tablet protease-inhibitors [Roche]). The bacteria were lysed by sonication and the supernatant was cleared by centrifugation at 16,500 rpm for 30 min at 4ºC.

The clarified supernatant was loaded onto a HisTrap FF column (Cytiva) using a peristaltic pump and washed with 10 column volumes of lysis buffer. The loaded column was then transferred to an ÄKTA System FPLC (Cytiva) and washed with an additional 10 column volumes of lysis buffer. Protein was eluted in a single step using elution buffer (the lysis buffer supplemented with 400 mM imidazole). Following elution, the sample was concentrated down to 0.5 mL using a 30 kDa concentrator (Amicon) and loaded onto a HiTrap desalting column (Cytiva), eluting with gel-filtration buffer (25 mM tris, pH 8.0, 150 mM NaCl, 1 mM tris(2-carboxyethyl)phosphine and 5% glycerol). The sample was then diluted to 20 mL, combined with 25 units of SUMO protease (Sigma-Aldrich), and incubated overnight at 4ºC.

Cleaved protein was loaded onto a HisTrap FF column (Cytiva). The protein was eluted with lysis buffer: although the protein no longer had the hexahistidine tag, PH domains have slight affinity for the Ni-NTA column and do not elute with the flow-through. The eluted protein was concentrated using a 10 kDa concentrator (Cytiva) down to 0.5 mL and loaded onto an Superdex 75 Increase 10/300 GL (Cytiva). The major peak, eluting at ~56 mL was collected and concentrated using a 10 kDa concentrator to ~30 μM, flash frozen in liquid nitrogen, and stored. Typical yields were 1–2 nmol.

Supported-lipid bilayer preparation

Supported-lipid bilayers were prepared essentially as described (Nocka et al., 2023) with slight modification. Lipids were prepared by mixing 96% 18:1 1,2-dioleoyl-sin-glycero-3-phosphocholine (DOPC) (Avanti Polar Lipids) and either 4% PIP_3 (Echelon Biosciences, Inc) or 4% PIP_2 (Brain PI(4,5)P2, Avanti) in an etched 50 mL round-bottom flask. To assess lipid quality, 0.005% TRITC-DHPE (Biotium) was added. PIP_3 was dissolved in a mixture of 1:2:0.8 chloroform to methanol to water just prior to use.

The solvent from the mixture was evaporated using rotary evaporation and then further dried under nitrogen for 15 min. Dried lipids were stored overnight at 4ºC. The next morning, lipids were rehydrated by dissolving to 1 mg/mL in water by vortexing. Small unilamellar vesicles (SUVs) were prepared by sonication (Analis Ultrasonic Processor 750 watt, 20 kHz) at 33% power, 20 s on, 50 s off for a total of 1 min 40 s active sonication. SUVs were then diluted to 0.25 mg/mL in 0.5x tris buffered saline and assessed for uniformity and size using dynamic light scattering (Brookhaven Instrument Corporation).

80 µL of the SUV mixture was added to each well of an etched glass slide mounted onto a Sticky Slide VI 0.4 (Ibidi GMBH) and incubated for 30 min at room temperature. Each well was then washed with 1x hanks balanced salt solution (HBSS) under vacuum as described (Nocka et al., 2023), then blocked for 10 min with β-Casein (0.1% w/v in HBSS) and washed again with 1x HBSS. Slides were then washed with imaging buffer (HBSS with 0.01% w/v β-Casein).

To image protein binding, 100 µL of imaging buffer were removed from the chamber (total volume 200 µL) and replaced with 100 µL of sample at the indicated times before

acquisition. For single-molecule measurements and FCS, a scavenging mixture (10x: 100 μM β-mercaptoethanol, 20 mM Trolox, 3.2 mg/mL glucose oxidase [Serva Electrophoresis GMBH]) was prepared. This mixture was diluted 10-fold into the sample just before addition to the imaging chamber and imaging.

TIRF imaging

TIRF microscopy was performed as described (Chung et al., 2019; Nocka et al., 2023). Briefly, images were collected on a Nikon Eclipse Ti-inverted microscope (Nikon, Tokyo, Japan) with a 100 x TIRF objective (NA 1.49) and an Andor iXon electron-multiplying charge-coupled device (EMCCD) camera (Oxford Instruments). Lasers (488 and 561 nm; Coherent, Inc.) were used as illumination sources.

Fluorescence correlation spectroscopy and analysis

FCS was performed as described (Chung et al., 2016). Briefly, FCS was performed on a modified inverted microscope (Nikon TE2000), excited using bandpassed wavelengths from a white-light laser source (SuperK Extreme EXW-12, NKT Photonics, Copenhagen, Denmark). A 100x oil-immersion objective was used and signal was recorded with an avalanche photodiode detector (Hamamatsu). The signal was converted into autocorrelation signal by a digital correlator. Fitting to a 2D diffusion model was performed as previously described (Chung et al., 2019).

Kinetic Modeling

Kinetic modeling was performed as previously described (Eisen et al., 2020). Briefly, a set of differential equations describing the reaction scheme were constructed in R and solved using deSolve (Soetaert et al., 2010). Summary statistics and plotting were performed using ggplot2 (Wickham, 2009).

Western blotting

Western blotting was performed as described (Nocka et al., 2023). Blots were probed with a rabbit monoclonal antibody targeting BTK (Cell Signaling Technology #3533). For a loading control, blots were probed with a rabbit polyclonal antibody targeting 14-3-3 (Cell Signaling Technology #8312).

Acknowledgments

We thank L. Nocka and S. Choi for helpful discussion, along with other members of the Kuriyan, Groves, and Weiss laboratories. We appreciate the technical advice of M. West, K. Pestal, H. Ren and W-L. Lo.

Funding

T.J.E. is a Damon Runyon Fellow supported by the Damon Runyon Cancer Research Foundation (DRG-2429–21). J.K. and A.W. were investigators with the Howard Hughes Medical Institute. This work was supported by the National Institutes of Health (P01 A1091580).

Author Contributions

T.J.E, A.W., and J.K. conceived the project and designed the study. T.J.E. and S.G. performed the experiments. T.J.E. wrote the paper, with review and editing from all authors.

Competing interests

John Kuriyan and Arthur Weiss are co-founders of Nurix Therapeutics.

Data and materials availability

Raw fastq files and processed files are available on DRYAD. Code for generating saturation-mutagenesis libraries and analyzing them is available on Github (https://github.com/timeisen/MutagenesisPlotCode).

References

Aryal, M., Lin, D., Regan, K., Du, S., Shi, H., Alvarado, J.J., Ilina, T.V., Andreotti, A.H., and Smithgall, T.E. (2022). The HIV-1 protein Nef activates the Tec family kinase Btk by stabilizing an intermolecular SH3-SH2 domain interaction. Sci Signal *15*, eabn8359.

Baba, Y., Hashimoto, S., Matsushita, M., Watanabe, D., Kishimoto, T., Kurosaki, T., and Tsukada, S. (2001). BLNK mediates Syk-dependent Btk activation. Proc Natl Acad Sci U S A *98*, 2582-2586.

Bender, A.T., Gardberg, A., Pereira, A., Johnson, T., Wu, Y., Grenningloh, R., Head, J., Morandi, F., Haselmayer, P., and Liu-Bujalski, L. (2017). Ability of Bruton's tyrosine kinase inhibitors to sequester Y551 and prevent phosphorylation determines potency for inhibition of Fc receptor but not B-cell receptor signaling. Molecular Pharmacology *91*, 208-219.

Bray, N.L., Pimentel, H., Melsted, P., and Pachter, L. (2016). Near-optimal probabilistic RNA-seq quantification. Nat Biotechnol *34*, 525-527.

Chu, V.T., Weber, T., Wefers, B., Wurst, W., Sander, S., Rajewsky, K., and Kuhn, R. (2015). Increasing the efficiency of homology-directed repair for CRISPR-Cas9-induced precise gene editing in mammalian cells. Nat Biotechnol *33*, 543-548.

Chung, J.K., Lee, Y.K., Lam, H.Y.M., and Groves, J.T. (2016). Covalent Ras Dimerization on Membrane Surfaces through Photosensitized Oxidation. Journal of the American Chemical Society *138*, 1800-1803.

Chung, J.K., Nocka, L.M., Decker, A., Wang, Q., Kadlecek, T.A., Weiss, A., Kuriyan, J., and Groves, J.T. (2019). Switch-like activation of Bruton's tyrosine kinase by membrane-mediated dimerization. Proceedings of the National Academy of Sciences of the United States of America *166*, 10798-10803.

Cibrian, D., and Sanchez-Madrid, F. (2017). CD69: from activation marker to metabolic gatekeeper. Eur J Immunol *47*, 946-953.

Coyote-Maestas, W., Nedrud, D., Suma, A., He, Y., Matreyek, K.A., Fowler, D.M., Carnevale, V., Myers, C.L., and Schmidt, D. (2021). Probing ion channel functional architecture and domain recombination compatibility by massively parallel domain insertion profiling. Nat Commun *12*, 7114.

Dal Porto, J.M., Gauld, S.B., Merrell, K.T., Mills, D., Pugh-Bernard, A.E., and Cambier, J. (2004). B cell antigen receptor signaling 101. Mol Immunol *41*, 599-613.

Deindl, S., Kadlecek, T.A., Brdicka, T., Cao, X., Weiss, A., and Kuriyan, J. (2007). Structural Basis for the Inhibition of Tyrosine Kinase Activity of ZAP-70. Cell *129*, 735-746.

Dhami, K., Chakraborty, A., Gururaja, T.L., Cheung, L.W., Sun, C., DeAnda, F., and Huang, X. (2022). Kinase-deficient BTK mutants confer ibrutinib resistance through activation of the kinase HCK. Sci Signal *15*, eabg5216.

Du, Z., and Lovly, C.M. (2018). Mechanisms of receptor tyrosine kinase activation in cancer. Mol Cancer *17*, 58.

Eisen, T.J., Eichhorn, S.W., Subtelny, A.O., Lin, K.S., McGeary, S.E., Gupta, S., and Bartel, D.P. (2020). The Dynamics of Cytoplasmic mRNA Metabolism. Mol Cell *77*, 786-799 e710.

Ershov, D., Phan, M.S., Pylvanainen, J.W., Rigaud, S.U., Le Blanc, L., Charles-Orszag, A., Conway, J.R.W., Laine, R.F., Roy, N.H., Bonazzi, D.*, et al.* (2022). TrackMate 7: integrating state-of-the-art segmentation algorithms into tracking pipelines. Nat Methods *19*, 829-+.

Fluckiger, A.C., Li, Z., Kato, R.M., Wahl, M.I., Ochs, H.D., Longnecker, R., Kinet, J.P., Witte, O.N., Scharenberg, A.M., and Rawlings, D.J. (1998). Btk/Tec kinases regulate sustained increases in intracellular Ca2+ following B-cell receptor activation. EMBO Journal *17*, 1973-1985.

Fukuda, M., Kojima, T., Kabayama, H., and Mikoshiba, K. (1996). Mutation of the pleckstrin homology domain of Bruton's tyrosine kinase in immunodeficiency impaired inositol 1,3,4,5-tetrakisphosphate binding capacity. J Biol Chem *271*, 30303-30306.

Gibbs, C.S., and Zoller, M.J. (1991). Rational scanning mutagenesis of a protein kinase identifies functional regions involved in catalysis and substrate interactions. J Biol Chem *266*, 8923-8931.

Hanson, G., and Coller, J. (2018). Codon optimality, bias and usage in translation and mRNA decay. Nat Rev Mol Cell Biol *19*, 20-30.

Haselmayer, P., Camps, M., Liu-Bujalski, L., Nguyen, N., Morandi, F., Head, J., O'Mahony, A., Zimmerli, S.C., Bruns, L., Bender, A.T.*, et al.* (2019). Efficacy and Pharmacodynamic Modeling of the BTK Inhibitor Evobrutinib in Autoimmune Disease Models. J Immunol *202*, 2888-2906.

Hendriks, R.W., Yuvaraj, S., and Kil, L.P. (2014). Targeting Bruton's tyrosine kinase in B cell malignancies. Nat Rev Cancer *14*, 219-232.

Herbst, S., Shah, A., Mazon Moya, M., Marzola, V., Jensen, B., Reed, A., Birrell, M.A., Saijo, S., Mostowy, S., Shaunak, S.*, et al.* (2015). Phagocytosis-dependent activation of a TLR9-BTK-calcineurin-NFAT pathway co-ordinates innate immunity to Aspergillus fumigatus. EMBO Mol Med *7*, 240-258.

Hidalgo, F., Nocka, L.M., Shah, N.H., Gorday, K., Latorraca, N.R., Bandaru, P., Templeton, S., Lee, D., Karandur, D., Pelton, J.G.*, et al.* (2022). A saturation-mutagenesis analysis of the interplay between stability and activation in Ras. Elife *11*.

Holm, L. (2022). Dali server: structural unification of protein families. Nucleic Acids Res *50*, W210-W215.

Hubbard, S.R. (1997). Crystal structure of the activated insulin receptor tyrosine kinase in complex with peptide substrate and ATP analog. EMBO J *16*, 5572-5581.

Huse, M., and Kuriyan, J. (2002). The conformational plasticity of protein kinases. Cell *109*, 275-282.

Hyvönen, M., and Saraste, M. (1997). Stucture of the PH domain and Btk motif from Bruton's tyrosine kinase: Molecular explanations for X-linked agammaglobulinaemia. EMBO Journal *16*, 3396-3404.

Johnson, L.N., Noble, M.E., and Owen, D.J. (1996). Active and inactive protein kinases: structural basis for regulation. Cell *85*, 149-158.

Joseph, R.E., Kleino, I., Wales, T.E., Xie, Q., Fulton, D.B., Engen, J.R., Berg, L.J., and Andreotti, A.H. (2013). Activation loop dynamics determine the different catalytic efficiencies of B cell- and T cell-specific tec kinases. Science Signaling *6*, 1-13.

Jumper, J., Evans, R., Pritzel, A., Green, T., Figurnov, M., Ronneberger, O., Tunyasuvunakool, K., Bates, R., Zidek, A., Potapenko, A.*, et al.* (2021). Highly accurate protein structure prediction with AlphaFold. Nature *596*, 583-589.

Kim, Y.J., Sekiya, F., Poulin, B., Bae, Y.S., and Rhee, S.G. (2004). Mechanism of B-cell receptor-induced phosphorylation and activation of phospholipase C-gamma2. Mol Cell Biol *24*, 9986-9999.

Klein, G., Giovanella, B., Westman, A., Stehlin, J.S., and Mumford, D. (1975). An EBV-genome-negative cell line established from an American Burkitt lymphoma; receptor characteristics. EBV infectibility and permanent conversion into EBV-positive sublines by in vitro infection. Intervirology *5*, 319-334.

Koretzky, G.A., Abtahian, F., and Silverman, M.A. (2006). SLP76 and SLP65: complex regulation of signalling in lymphocytes and beyond. Nat Rev Immunol *6*, 67-78.

Landego, I., Jayachandran, N., Wullschleger, S., Zhang, T.T., Gibson, I.W., Miller, A., Alessi, D.R., and Marshall, A.J. (2012). Interaction of TAPP adapter proteins with phosphatidylinositol (3,4)-bisphosphate regulates B-cell activation and autoantibody production. Eur J Immunol *42*, 2760-2770.

Le Huray, K.I.P., Wang, H., Sobott, F., and Kalli, A.C. (2022). Systematic simulation of the interactions of pleckstrin homology domains with membranes. Sci Adv *8*, eabn6992.

Lemmon, M.A., and Ferguson, K.M. (2000). Signal-dependent membrane targeting by pleckstrin homology (PH) domains. Biochem J *350 Pt 1*, 1-18.

Lenoir, M., Kufareva, I., Abagyan, R., and Overduin, M. (2015). Membrane and Protein Interactions of the Pleckstrin Homology Domain Superfamily. Membranes (Basel) *5*, 646-663.

Li, T., Tsukada, S., Satterthwaite, A., Havlik, M.H., Park, H., Takatsu, K., and Witte, O.N. (1995). Activation of bruton's tyrosine kinase (BTK) by a point mutation in its pleckstrin homology (PH) domain. Immunity *2*, 451-460.

Lo, W.L., Shah, N.H., Rubin, S.A., Zhang, W.G., Horkova, V., Fallahee, I.R., Stepanek, O., Zon, L.I., Kuriyan, J., and Weiss, A. (2019). Slow phosphorylation of a tyrosine residue in LAT optimizes T cell ligand discrimination. Nature Immunology *20*, 1481-+.

Lykke-Andersen, S., and Jensen, T.H. (2015). Nonsense-mediated mRNA decay: an intricate machinery that shapes transcriptomes. Nat Rev Mol Cell Biol *16*, 665-677.

Maas, A., Dingjan, G.M., Grosveld, F., and Hendriks, R.W. (1999). Early arrest in B cell development in transgenic mice that express the E41K Bruton's tyrosine kinase mutant under the control of the CD19 promoter region. J Immunol *162*, 6526-6533.

Maloney, R.C., Zhang, M., Jang, H., and Nussinov, R. (2021). The mechanism of activation of monomeric B-Raf V600E. Comput Struct Biotechnol J *19*, 3349-3363.

Marshall, A.J., Krahn, A.K., Ma, K., Duronio, V., and Hou, S. (2002). TAPP1 and TAPP2 are targets of phosphatidylinositol 3-kinase signaling in B cells: sustained plasma membrane recruitment triggered by the B-cell antigen receptor. Mol Cell Biol *22*, 5479-5491.

Middendorp, S., Dingjan, G.M., Maas, A., Dahlenborg, K., and Hendriks, R.W. (2003). Function of Bruton's tyrosine kinase during B cell development is partially independent of its catalytic activity. J Immunol *171*, 5988-5996.

Muller, R., Meacham, Z.A., Ferguson, L., and Ingolia, N.T. (2020). CiBER-seq dissects genetic networks by quantitative CRISPRi profiling of expression phenotypes. Science *370*.

Nocka, L.M., Eisen, T.J., Iavarone, A.T., Groves, J.T., and Kuriyan, J. (2023). Stimulation of the catalytic activity of the tyrosine kinase Btk by the adaptor protein Grb2. Elife *12*.

Ortutay, C., Nore, B.F., Vihinen, M., and Smith, C.I.E. (2008). Chapter 3 Phylogeny of Tec Family Kinases. Identification of a Premetazoan Origin of Btk, Bmx, Itk, Tec, Txk, and the Btk Regulator SH3BP5, Vol 64, 1 edn (Elesvier Inc.).

Pal Singh, S., Dammeijer, F., and Hendriks, R.W. (2018). Role of Bruton's tyrosine kinase in B cells and malignancies. Molecular Cancer *17*, 1-23.

R Development Core Team (2022). R: A Language and Environment for Statistical Computing.

Shan, X., Czar, M.J., Bunnell, S.C., Liu, P., Liu, Y., Schwartzberg, P.L., and Wange, R.L. (2000). Deficiency of PTEN in Jurkat T cells causes constitutive localization of Itk to the plasma membrane and hyperresponsiveness to CD3 stimulation. Mol Cell Biol *20*, 6945-6957.

Soetaert, K., Petzoldt, T., and Setzer, R.W. (2010). Solving Differential Equations in R: Package deSolve. J Stat Softw *33*, 1-25.

Su, Y.W., Zhang, Y., Schweikert, J., Koretzky, G.A., Reth, M., and Wienands, J. (1999). Interaction of SLP adaptors with the SH2 domain of Tec family kinases. Eur J Immunol *29*, 3702-3711.

Subramanian, S., Gorday, K., Marcus, K., Orellana, M.R., Ren, P., Luo, X.R., O'Donnell, M.E., and Kuriyan, J. (2021). Allosteric communication in DNA polymerase clamp loaders relies on a critical hydrogen-bonded junction. Elife *10*.

Taneichi, H., Kanegane, H., Sira, M.M., Futatani, T., Agematsu, K., Sako, M., Kaneko, H., Kondo, N., Kaisho, T., and Miyawaki, T. (2008). Toll-like receptor signaling is impaired in dendritic cells from patients with X-linked agammaglobulinemia. Clin Immunol *126*, 148-154.

Thomas, C.C., Dowler, S., Deak, M., Alessi, D.R., and van Aalten, D.M. (2001). Crystal structure of the phosphatidylinositol 3,4-bisphosphate-binding pleckstrin homology (PH) domain of tandem PH-domain-containing protein 1 (TAPP1): molecular basis of lipid specificity. Biochem J *358*, 287-294.

Tomlinson, M.G., Kane, L.P., Su, J., Kadlecek, T.A., Mollenauer, M.N., and Weiss, A. (2004). Expression and Function of Tec, Itk, and Btk in Lymphocytes: Evidence for a Unique Role for Tec. Molecular and Cellular Biology *24*, 2455-2466.

Vetrie, D., Vorechovsky, I., Sideras, P., Holland, J., Davies, A., Flinter, F., Hammarstrom, L., Kinnon, C., Levinsky, R., Bobrow, M.*, et al.* (1993). The gene involved in X-linked agammaglobulinaemia is a member of the src family of protein-tyrosine kinases. Nature *361*, 226-233.

Wang, E., Mi, X., Thompson, M.C., Montoya, S., Notti, R.Q., Afaghani, J., Durham, B.H., Penson, A., Witkowski, M.T., Lu, S.X.*, et al.* (2022). Mechanisms of Resistance to Noncovalent Bruton's Tyrosine Kinase Inhibitors. N Engl J Med *386*, 735-743.

Wang, Q., Pechersky, Y., Sagawa, S., Pan, A.C., and Shaw, D.E. (2019a). Structural mechanism for Bruton's tyrosine kinase activation at the cell membrane. Proc Natl Acad Sci U S A *116*, 9390-9399.

Wang, Q., Vogan, E.M., Nocka, L.M., Rosen, C.E., Zorn, J.A., Harrison, S.C., and Kuriyan, J. (2015a). Autoinhibition of Bruton's tyrosine kinase (Btk) and activation by soluble inositol hexakisphosphate. eLife *2015*, 1-31.

Wang, S., Mondal, S., Zhao, C., Berishaj, M., Ghanakota, P., Batlevi, C.L., Dogan, A., Seshan, V.E., Abel, R., Green, M.R.*, et al.* (2019b). Noncovalent inhibitors reveal BTK gatekeeper and auto-inhibitory residues that control its transforming activity. JCI Insight *4*.

Wang, X., Huang, H., and Young, K.H. (2015b). The PTEN tumor suppressor gene and its role in lymphoma pathogenesis. Aging (Albany NY) *7*, 1032-1049.

Weber, A.N.R., Bittner, Z., Liu, X., Dang, T.M., Radsak, M.P., and Brunner, C. (2017). Bruton's Tyrosine Kinase: An Emerging Key Player in Innate Immunity. Front Immunol *8*, 1454.

Weiss, A., and Stobo, J.D. (1984). Requirement for the coexpression of T3 and the T cell antigen receptor on a malignant human T cell line. J Exp Med *160*, 1284-1299.

Weiss, A., Wiskocil, R.L., and Stobo, J.D. (1984). The role of T3 surface molecules in the activation of human T cells: a two-stimulus requirement for IL 2 production reflects events occurring at a pre-translational level. J Immunol *133*, 123-128.

Wickham, H. (2009). ggplot2: Elegant Graphics for Data Analysis. Use R, 1-212.

Wu, F., Zhao, J., Chen, L., Liu, X., Su, P., Han, Y., Feng, B., and Li, Q. (2012). A novel BTK-like protein involved in immune response in Lethenteron japonicum. Immunol Lett *146*, 57-63.

Xia, S., Liu, X., Cao, X., and Xu, S. (2020). T-cell expression of Bruton's tyrosine kinase promotes autoreactive T-cell activation and exacerbates aplastic anemia. Cell Mol Immunol *17*, 1042-1052.

Xu, B., English, J.M., Wilsbacher, J.L., Stippec, S., Goldsmith, E.J., and Cobb, M.H. (2000). WNK1, a novel mammalian serine/threonine protein kinase lacking the catalytic lysine in subdomain II. J Biol Chem *275*, 16795-16801.

Xu, Z., Stokoe, D., Kane, L.P., and Weiss, A. (2002). The inducible expression of the tumor suppressor gene PTEN promotes apoptosis and decreases cell size by inhibiting the PI3K/Akt pathway in Jurkat T cells. Cell Growth Differ *13*, 285-296.

Yablonski, D., and Weiss, A. (2001). Mechanisms of signaling by the hematopoietic-specific adaptor proteins, SLP-76 and LAT and their B cell counterpart, BLNK/SLP-65. Adv Immunol *79*, 93-128.

Yuan, H., Zhu, Y., Cheng, Y., Hou, J., Jin, F., Li, M., Jia, W., Cheng, Z., Xing, H., Liu, M.*, et al.* (2022). BTK kinase activity is dispensable for the survival of diffuse large B-cell lymphoma. J Biol Chem *298*, 102555.

Main-text figure legends

Figure 1. Evolution of the Saraste dimer interface.

(A) Crystal structure of the Saraste dimer of the BTK PH–TH module (PDB: 1BTK). Loops S1 (residues 41–51) and S2 (residues 91–100) are shown in orange. Note that the insertion (residues 79–99, Figure 1B) encompasses more than just the S2 loop. (left) The membrane is shown as a dashed line. (right) The model is shown as if looking down through the membrane from the extracellular side. (B) (left) A gene phylogenetic tree of BTK homologs. 366 sequences of BTK in representative vertebrates are shown, downloaded from HomoloGene (NCBI). The tree is rooted using the lamprey (*Lethenteron camtschaticum*) Tec kinase. Vertebrate classes are shown as a single color. (right) Homologs that have any sequence that aligns to residues 79–99 (IPRRGEESSEMEQISIIERFP) from human BTK are denoted with an X. Others only have gaps in this region.

Figure 2. A high-through mutagenesis assay for BTK function in B cells and T cells

(A) BTK induces CD69 expression in Ramos cells. The percentage of the population that expresses CD69, measured by FACS, is shown. Cell populations were transduced four days before sorting with lentiviruses expressing EGFP or human BTK. The panel at left is without stimulation. At right, the cells were stimulated with anti-IgM (μ chain) for 16 h at 10 μg/mL. Shown is the mean ± standard error from three replicates. N.S: not significant, *$p < 0.05$, **$p < 0.01$, ***$p < 0.001$, t test. (B) BTK-deficient Ramos cells induce CD69 expression in response to stimulation, and exhibit increased CD69 upon expression of human BTK without stimulation. Otherwise as in (A). (C) BTK induces CD69 expression in Jurkat cells. The cells were left unstimulated (left) or stimulated (right) with 1 μg/mL anti-T cell receptor antibody C305 for 16

h. Shown is the mean ± standard error from four replicates. (D) ITK-deficient Jurkat cells induce CD69 expression in response to stimulation, and exhibit increased CD69 upon expression of human BTK without stimulation. Otherwise as in (A). (E) The effects of mutations at Glu^{41} agree with previous studies. Mean fitness values ± standard error for biological triplicates are shown (y axis) for all possible amino acid substitutions (x axis). X represents the average value for two stop codons, averaged over the three replicates. The wild-type residue is shown in blue, with the residue single-letter code and human numbering shown above the block of substitutions.

Figure 3. PH–TH dimerization is dispensable in Ramos B cells.

(A) The hydrophobic residues that constitute the Saraste dimer interface. PH–TH dimer interface residues are shown as sticks on a cartoon representation of the dimer interface, with the two protomers shown in different colors (PDB: 1BTK). (B) Sensitivity of the PH–TH dimer interface mutations in Ramos cells. For each residue shown in (A), fitness scores for all possible mutations at that position are shown. Tyr^{42} and Phe^{44} values are from the S1-loop library. Ile^{92} and Ile^{95} are from the S2-loop library (key). Otherwise as in Figure 2E.

Figure 4. Kinase activity is required for BTK signaling in Jurkat T cells.

(A) The HRD motif is sensitive to mutation in Jurkat cells. Fitness scores for all possible substitutions in the HRD motif are shown, with the residue code and number above each block of mutations. N = 4 biological replicates. Otherwise as in Figure 2E. (B) Mutations in the phospho-regulated tyrosine Tyr^{551} in the activation-loop are not tolerated. Otherwise as in (A), except plotting values from the activation-loop library. (C) Leu^{547}, when mutated to proline, is

activating. Otherwise as in (B). (D) Tyr^{545}, at the equivalent position as Val^{600} in BRAF kinase, increases BTK activity when mutated to many residues. Otherwise as in (B).

Figure 5. PH–TH dimerization is required for signaling in Jurkat T cells.

(A) Agreement between fitness scores between the Ramos B cell and Jurkat T cell for the S1 and S2-loop libraries. Mean fitness scores ± standard error for n = 441 substitutions in the two libraries are plotted for both cell lines. Dashed lines indicate x = 0, y = 0, and y = x. (B) The dimer interface is sensitive in Jurkat cells. Otherwise as in Figure 3B, except showing data for Jurkat cells with n = 4 biological replicates. (C) Both the S1 and S2 loops are required for signaling in Jurkat T cells. Lentiviruses expressing human BTK without the S1 loop (residues 41–51, "S1 mutant") or the S2 loop (residues 91–100, "S2 mutant") were used to transduced ITK-deficient Jurkat T cells. The mean fraction of CD69-positive cells ± standard error, determined by FACS, is shown for n = 6 replicates. N.S: not significant, *$p < 0.05$, **$p < 0.01$, ***$p < 0.001$, t test. (D) The S2 loop is dispensable in Ramos B cells. Otherwise as in (E), except for n = 3 replicates.

Figure 6. The canonical PIP_3-binding site is sensitive to mutation but the peripheral site is tolerant.

(A) The residues that constitute the canonical site are sensitive to mutation. Fitness scores for all substitutions for each residue that interacts with the lipid are shown. Otherwise as in Figure 2E. (B) The crystal structure (PDB: 4Y94) of the PH–TH module of BTK is shown as a cartoon. The two protomers of the dimer are shown in cyan and pink, with the canonical-site interacting residues shown as stick representation on one of the two protomers. The lipid crystallized in this

structure, hexakisphosphate (IP_6) is shown as stick representation. (C) The residues of the peripheral site tolerate mutation. Fitness scores for all possible substitutions for each residue that interacts with the peripheral-site lipid are shown. Otherwise as in (A). (D) Crystal structure of the PH–TH module of BTK with the peripheral-site residues shown as stick representation. Otherwise as in (B).

Figure 7. Substitutions of positively charged residues near the plasma membrane have differential fitness effects.

(A) A set of mutations that show differential fitness in Ramos and Jurkat cells. Fitness scores in Jurkat cells (blue) are shown alongside fitness scores in Ramos cells (red) for lysine and arginine substitutions at select positions in the S1 loop. (B) Positioning of the residues that exhibit differential fitness. Stick representation of residues that change their fitness in the two cell lines (PDB: 1BTK). Note that Gly^{47} and Gly^{50} are not shown because they have no side chains. The positioning of the plasma membrane is indicated by a dashed line.

Figure 8. The mutation E45K increases the ability of monomeric BTK to bind membranes but decreases dimerization.

(A) Schematic of the adsorption assay. Purified PH–TH modules with a C-terminal EGFP tag adsorbed onto supported-lipid bilayers containing either 4% PIP_3 or 4% PIP_2 and 96% DOPC. Adsorption was visualized with TIRF microscopy which excites only the membrane-bound molecules. (B) PH–TH^{E45K} at low concentrations adsorbs more than PH–TH^{WT} to bilayers containing 4% PIP_3. The mean ± standard deviation number of molecules adsorbed after incubating 5 pM of protein (PH–TH^{WT}, PH–TH^{E45K}, PH–TH^{Y42K}) for 10 min was measured

using trackmate (Ershov et al., 2022) in Fiji. N = 4 trials. N.S: not significant, *$p < 0.05$, **$p < 0.01$, ***$p < 0.001$, t test. (C) PH–TH^{E45K} adsorbs more than PH–TH^{WT} to bilayers containing 4% PIP_2. Otherwise as in (B). (D) PH–TH^{E45K} adsorbs less than PH–TH^{WT} to bilayers containing 4% PIP_3 at high solution concentrations. Average TIRF intensity across the imaging field was measured after injection of 100 pM PH–TH^{E45K} or PH–TH^{WT} (key). The vertical dashed line represents the time at which the protein was injected. The different curves represent independent trials (n = 2 for wild-type, n = 3 for E45K). (E) PH–TH^{E45K} at high concentrations adsorbs more than PH–TH^{WT} to bilayers containing 4% PIP_2. Otherwise as in (D). (F) PH–TH^{E45K} exhibits faster diffusion than PH–TH^{WT} at high surface densities. The diffusion rate (y axis) was measured for different protein densities on 4% PIP_3-containing bilayers (x axis) using fluorescence correlation spectroscopy. Measurements were performed for PH–TH^{WT} and PH–TH^{E45K} in two independent experiments (key). (G) A model for how the mutation E45K changes the rate constants associated with monomer adsorption and dimerization.

Supplemental figure legends

Figure S1. An assay for BTK fitness in Ramos B cells.

(A) Western blot of BTK-knockout Ramos B-cell lines. The presence of BTK is indicated by the top band in the top blot for 14 CRISPR-targeted cell lines. Two of the lines used a non-targeting guide (NTC) and 12 of these used a guide targeting BTK exon 3. The cell numbers were not normalized prior to blotting: many of these lines failed to grow enough to produce signal, as judged by a loading control (anti-14-3-3, bottom blot). The BTK-deficient line 3-2-G2 was used in this study. (B) Ibrutinib decreases the BTK-dependent increase in CD69. ITK-deficient Jurkat cells were transduced with lentiviruses encoding human BTK or EGFP as in Figure 2C and then treated with ibrutinib at the indicated concentrations two days before sorting. Otherwise as in Figure 2C. (C) Ibrutinib decreases the stimulation and BTK-dependent CD69 expression. Otherwise as in (B). (D) Schematic showing the manipulations performed for screening Ramos cells for BTK function. BTK-deficient Ramos cells were transduced with viruses encoding wild-type BTK and mutations, and grown, and then sorted for CD69. (E) Stop codons are depleted in the input libraries in the Ramos-cell assay. The normalized read counts corresponding to codon substitutions at any position in the S1-loop library (left panel) or S2-loop library (right panel) in Ramos cells, shown as mean ± standard deviation for each of three replicates. The normalization is the raw read counts divided by the total number of reads in the library. The codons are ranked by the increasing order of read counts, and stop codons are shown in blue. (F) Stop codons are depleted in the input libraries in the Jurkat cell assay. Otherwise as in (E), using with n = 4 biological replicates.

Figure S2. Stimulation promotes BTK-independent singaling in ITK-deficient Jurkat cells and BTK-deficient Ramos cells

(A) The fraction of CD69 positive ITK-deficient Jurkat cells as a function of increasing concentration of the anti-T cell receptor antibody C305, as measured by FACS. The percentages are shown for two sort gates: EGFP-positive cells are those that were transduced with the lentivirus expressing human BTK-IRES-EGFP, and EGFP-negative are untransduced cells. Points represent the measured values, and the line is a fit to a binding-isotherm model. (B) Fitness scores for all variants in the S1-loop library over increasing concentrations of C305. For each of the points in (A), mRNA-seq libraries were prepared from the input (unsorted) and CD69-sorted fractions of cells. The fitness values for the wild-type sequences (blue), sequences with a mutation (red), or sequences with a stop codon (key) are plotted as a histogram (key). The values above each histogram indicate the concentration of C305, in μg/mL. Over increasing concentrations, the nonsense variants resemble the wild-type variants but the stop-codon variants do not. (C) A heatmap showing the fitness values (key) for each variant in the S1-loop library over different concentrations of C305. Variants were clustered by Euclidian distance using the hclust algorithm in R. (D) Pearson correlation values between biological replicates for the S1-loop library in Ramos B cells over increasing concentrations of anti-IgM stimulatory antibody.

Figure S3. BTK kinase activity is dispensable in Ramos cells.

(A) The HRD motif positions the catalytic base to abstract a proton from the peptide substrate. A crystal structure of the insulin receptor tyrosine kinase (PDB: 1IR3 (Hubbard, 1997)) in complex with phosphoaminophosphonic acid-adenylate ester. The histidine, arginine, and aspartate residues are shown as sticks (green) along with the ATP analog ANP (orange) and peptide

substrate (cyan). (B) The HRD motif tolerates mutations. Fitness scores showing all possible residue substitutions to the HRD motif in Ramos cells. Otherwise as in Figure 2E.

Figure S4. Jurkat cells exhibit strong dependence on the HRD segment.

Agreement of biological replicates. Fitness scores for n = 253 amino acid substitutions in the HRD-motif library are compared between biological quadruplicates. R is the Pearson correlation between each replicate, and the dashed line is y = x.

Figure S5. All mutations measured for the HRD and activation-loop libraries in Jurkat cells.

(A) Fitness scores for all positions in the HRD-motif library in Jurkat cells. Otherwise as in Figure 2E. (B) Fitness scores for all positions in the activation-loop library. Positions where the input read counts from all four replicates failed to pass the 50-read threshold are indicated with "N.D.". If two or three input replicates failed to pass the 50-read threshold, the mean value from the remaining one or two replicates is shown without an error bar. Otherwise as in (A).

Figure S6. Comparison of the S1 and S2 loop libraries between Ramos cells and Jurkat cells.

Fitness scores for all positions and mutations in the S1-loop library (A) or S2-loop library (B), showing the data from Jurkat cells (top row) and Ramos cells (bottom row). Otherwise as in Figure 2E.

Figure S7. All mutations investigated for the canonical-site and peripheral-site libraries in Jurkat cells.

Fitness scores for all positions in the canonical-site library (A) or peripheral-site library (B) in Jurkat cells. Otherwise as in Figure 2C. Position 37, originally designed as part of the canonical-site library, is excluded from this analysis entirely because of low read coverage for most of the substitutions.

Figure S8. Reconstituting PH–TH domain adsorption on supported-lipid bilayers.

(A) PH–TH^{WT}, PH–TH^{E45K}, and PH–TH^{Y42K} show the same rates of photobleaching. A histogram of the duration of the single-molecule tracks is shown for each variant (key), determined by trackmate in Fiji, on bilayers containing 4% PIP_3. (B) Diffusion rates are the same for the three variants. The distribution of distances between 20 ms imaging steps in tracks is shown for the three variants (key). PH–TH^{Y42K} shows a noisier distribution because it has fewer tracks, as it adsorbs less to the bilayer. The spots that did not move between adjacent frames (corresponding to a distance of 0) were omitted from this and other analyses. (C) PH–TH^{E45K} and PH–TH^{WT} have the same brightness per spot. A histogram of TIRF intensity for each spot in each track is shown for the three variants (key). (D) A sequence alignment of residues 39-51 in human BTK, aligned to ITK, TEC, and BMX. Alignment was performed using MUSCLE alignment software and manually edited. The figure was generated with AliView alignment viewer. Positions 41 and 45 are indicated. (E) PH–TH^{E45K} adsorbs less than PH–TH^{WT} to bilayers containing 4% PIP_3 at 250 pM solution concentration. PH–TH^{E45K} and PH–TH^{WT} proteins were incubated for 10 min on supported-lipid bilayers containing 4% PIP_3 and then the median TIRF intensity across the imaging field was measured. Dots represent independent imaging fields, with

the line (median), box (first and third quartiles) and whiskers (1.5x the interquartile range), with p*** < 0.001, t test. (F) The reaction scheme for kinetic modeling. (G) Kinetic modeling of PH–TH^{E45K} and PH–TH^{WT} proteins (key) at two different concentrations. The monomeric association (k_1) rate constant was 4.7 x 10^{-4} $pmol^{-1}sec^{-1}$ for both mutants (Chung et al., 2019) and the dimer dissociation rate constant (k_{-2}) was 5.0 x 10^{-4} sec^{-1} for both mutants. The monomeric disassociation (k_{-1}) rate constants were 1.5 and 1.5 x 10^{-4} sec^{-1} for PH–TH^{WT} and PH–TH^{E45K}, respectively. The dimeric association rate constant (k_2) was 100 $pmol^{-1}sec^{-}1$ and 0 $pmol^{-1}sec^{-}1$ for PH–TH^{WT} and PH–TH^{E45K}, respectively.

Figure 1

A

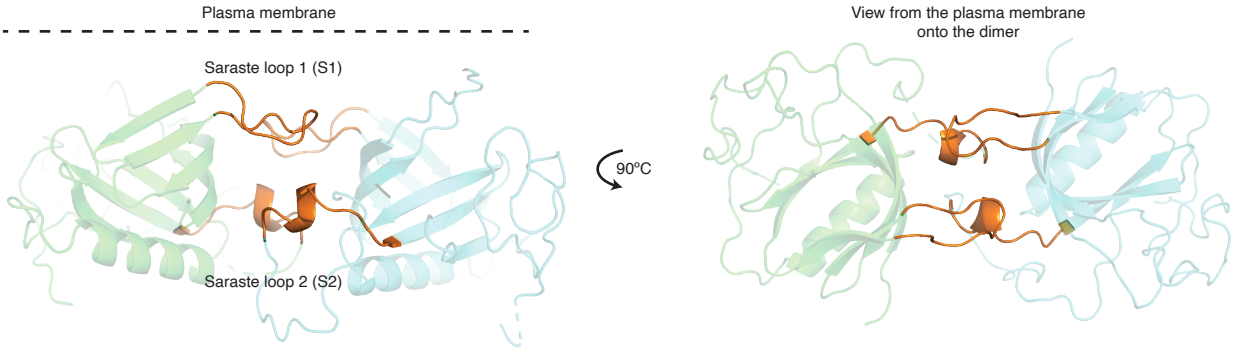
Plasma membrane
Saraste loop 1 (S1)
Saraste loop 2 (S2)
90ºC
View from the plasma membrane
onto the dimer

B

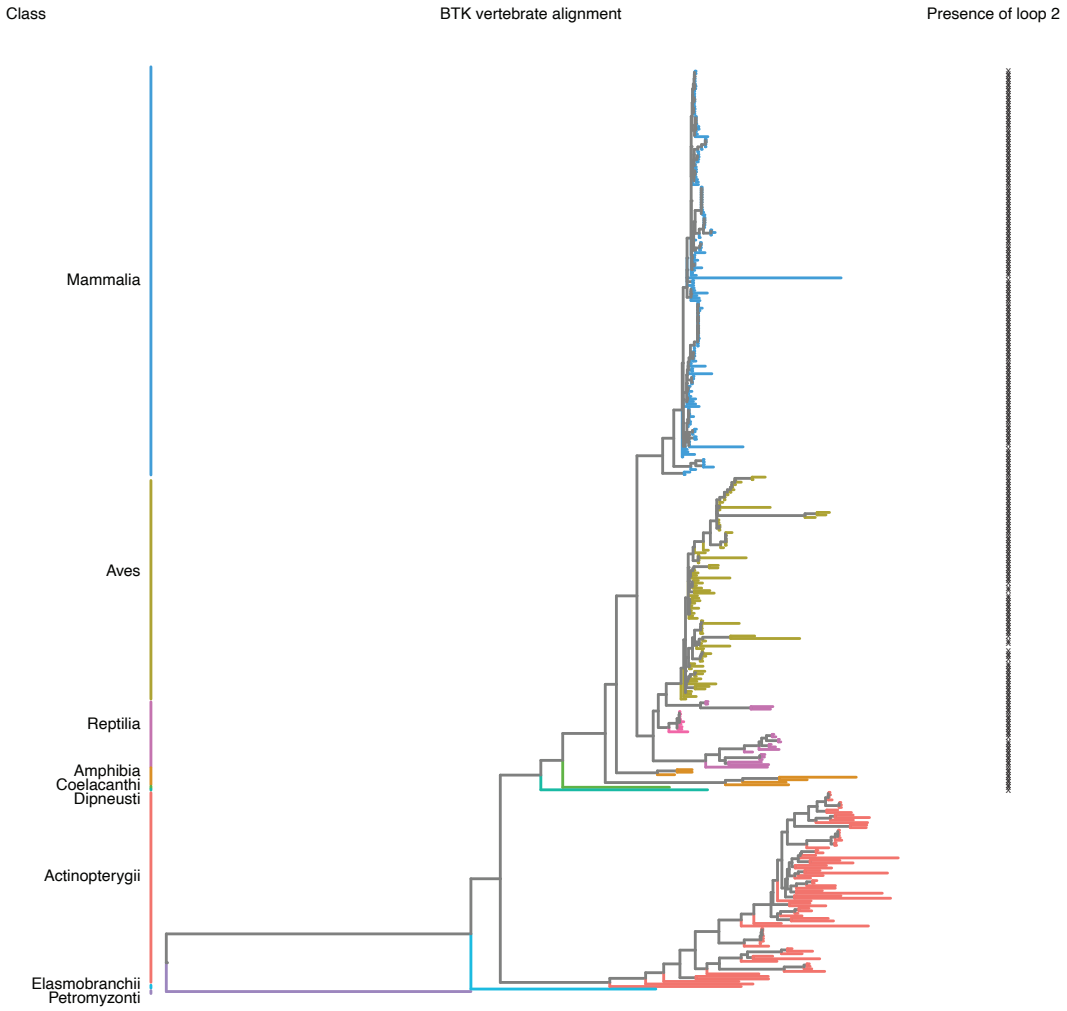
Class
BTK vertebrate alignment
Presence of loop 2
Mammalia
Aves
Reptilia
Amphibia
Coelacanthi
Dipneusti
Actinopterygii
Elasmobranchii
Petromyzonti

Figure 2

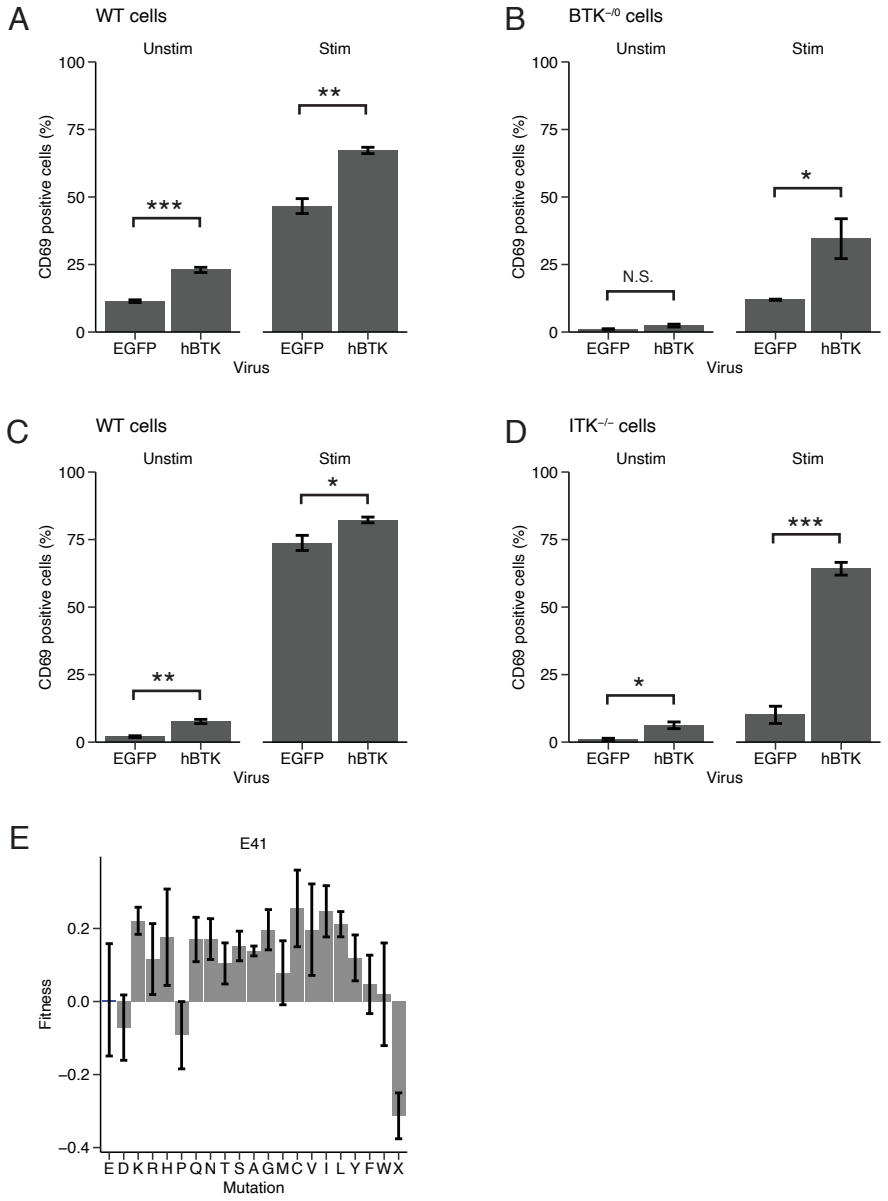
A
WT cells
Unstim
Stim
CD69 positive cells (%)
100
75
50
25
0
***
**
EGFP
hBTK
EGFP
hBTK
Virus
B
BTK−/0 cells
Unstim
Stim
CD69 positive cells (%)
N.S.
*
EGFP
hBTK
EGFP
hBTK
Virus
C
WT cells
Unstim
Stim
CD69 positive cells (%)
**
*
EGFP
hBTK
EGFP
hBTK
Virus
D
ITK−/− cells
Unstim
Stim
CD69 positive cells (%)
*
***
EGFP
hBTK
EGFP
hBTK
Virus
E
E41
Fitness
0.2
0.0
−0.2
−0.4
E D K R H P Q N T S A G M C V I L Y F W X
Mutation

Figure 3

A

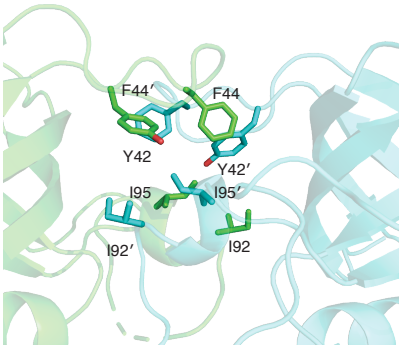
F44′
F44
Y42
Y42′
I95
I95′
I92′
I92

B

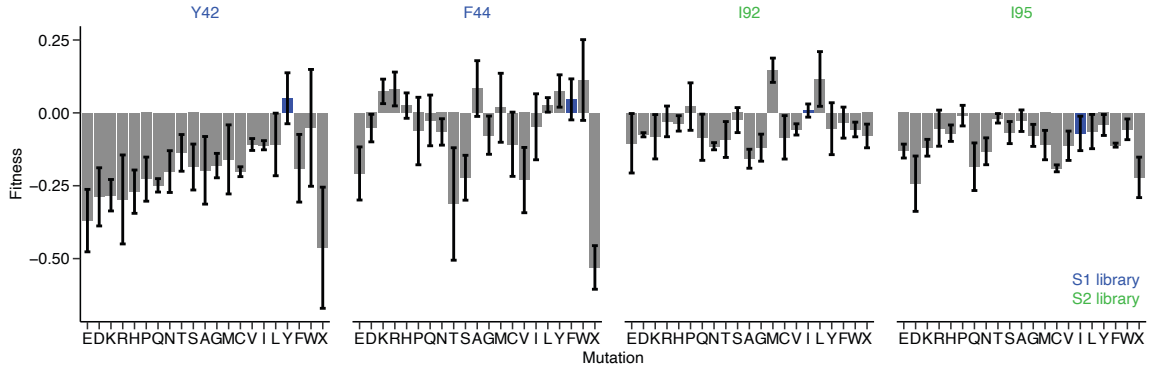
Y42
F44
I92
I95
0.25
0.00
−0.25
−0.50
Fitness
S1 library
S2 library
EDKRHPQNTSAGMCV I LYFWX
Mutation

Figure 4

A

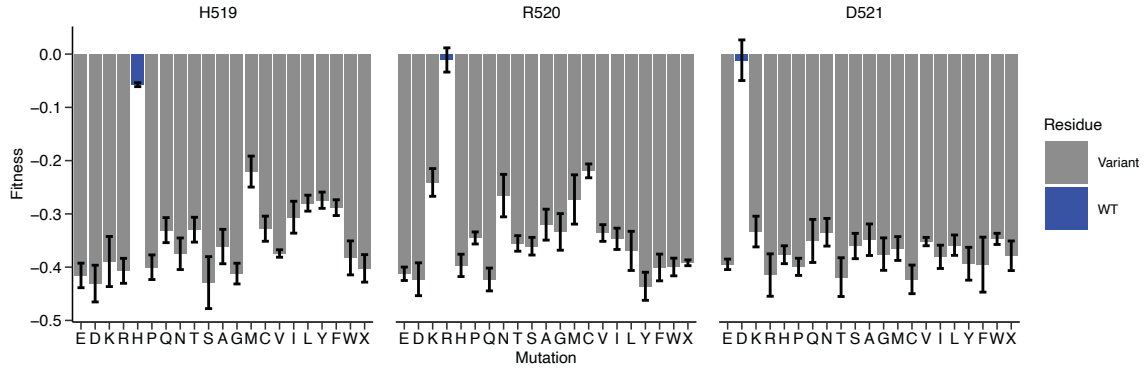

B

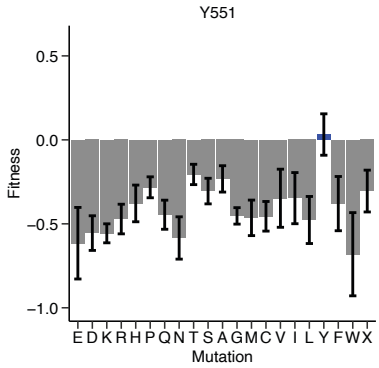

C

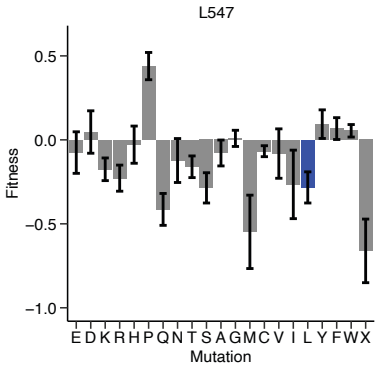

D

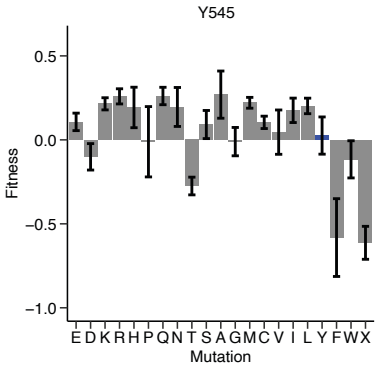

Figure 5

A

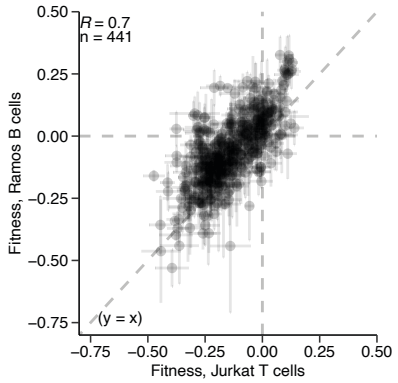

B

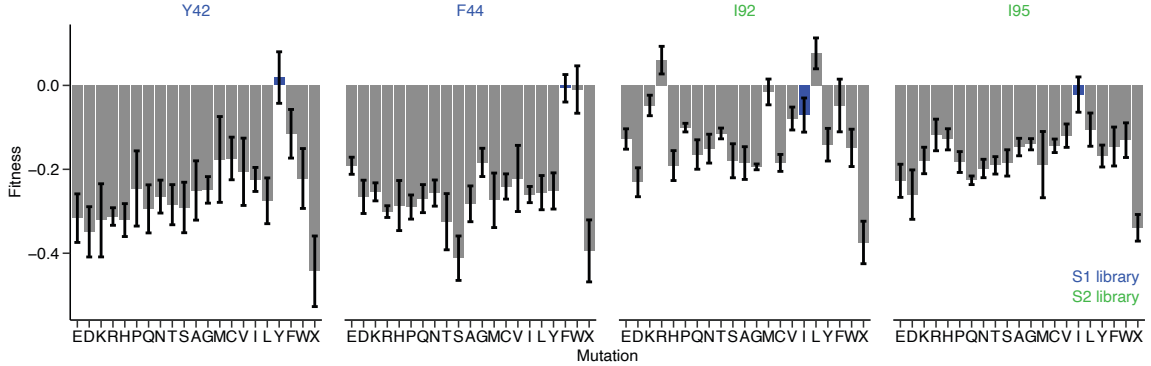

C

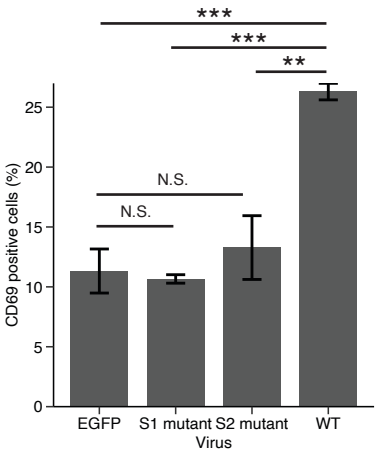

D

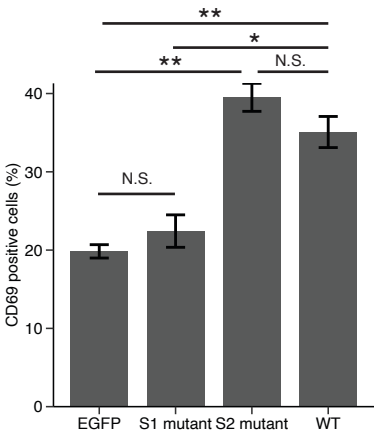

Figure 6

A

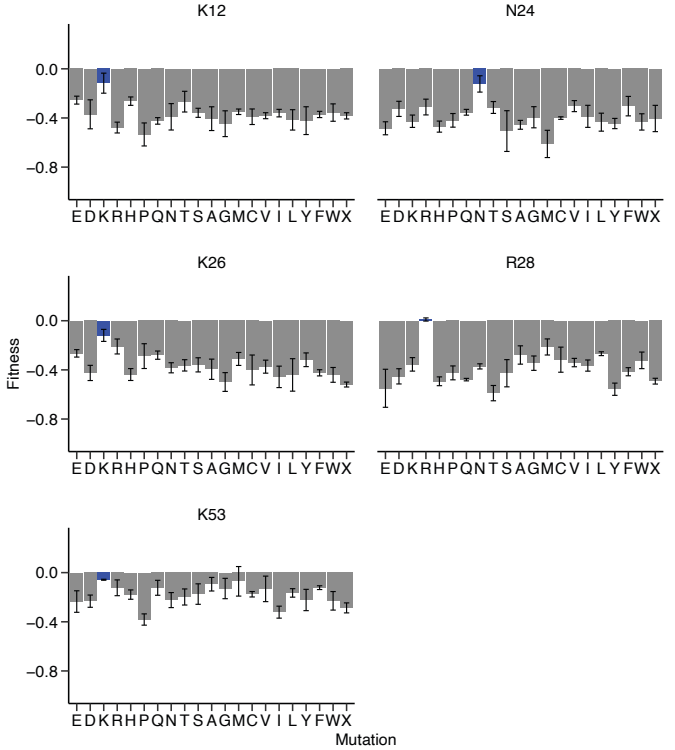

B

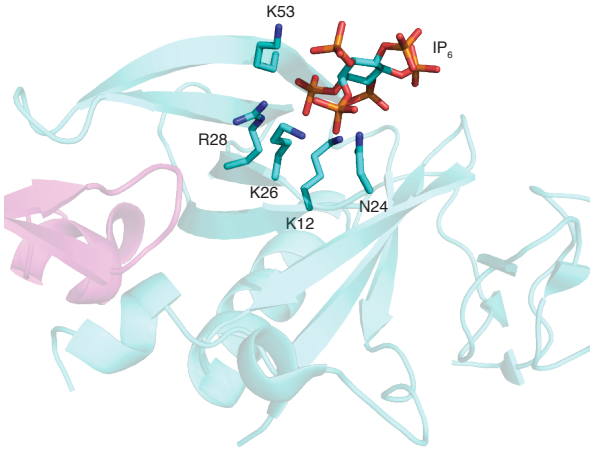

C

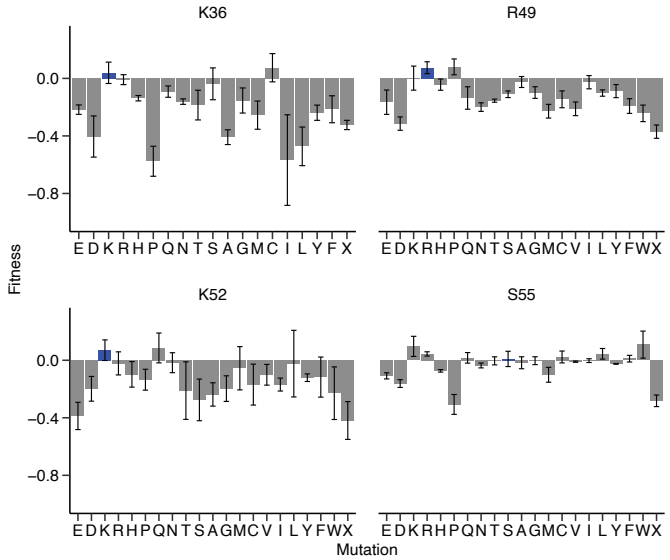

D

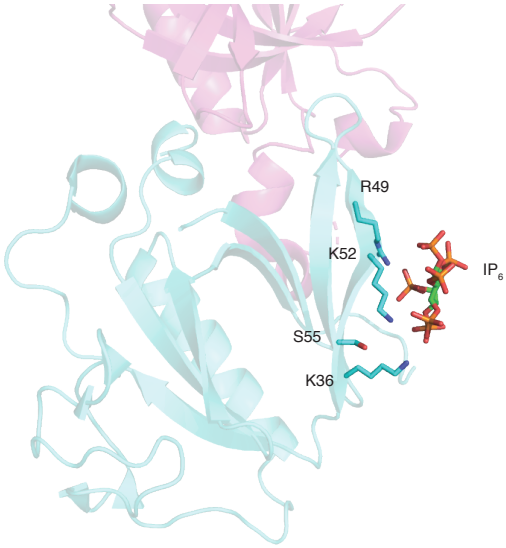

Figure 7

A

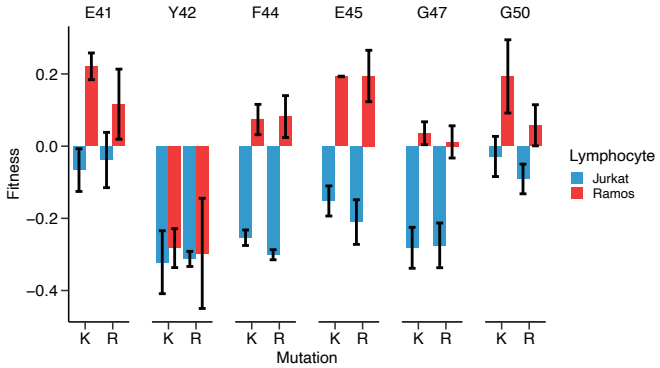
E41
Y42
F44
E45
G47
G50
0.2
0.0
−0.2
−0.4
Fitness
K R
Mutation
Lymphocyte
Jurkat
Ramos

B

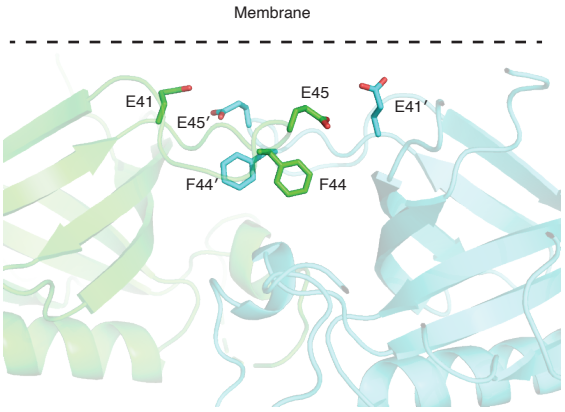
Membrane
E41
E45′
E45
E41′
F44′
F44

Figure 8

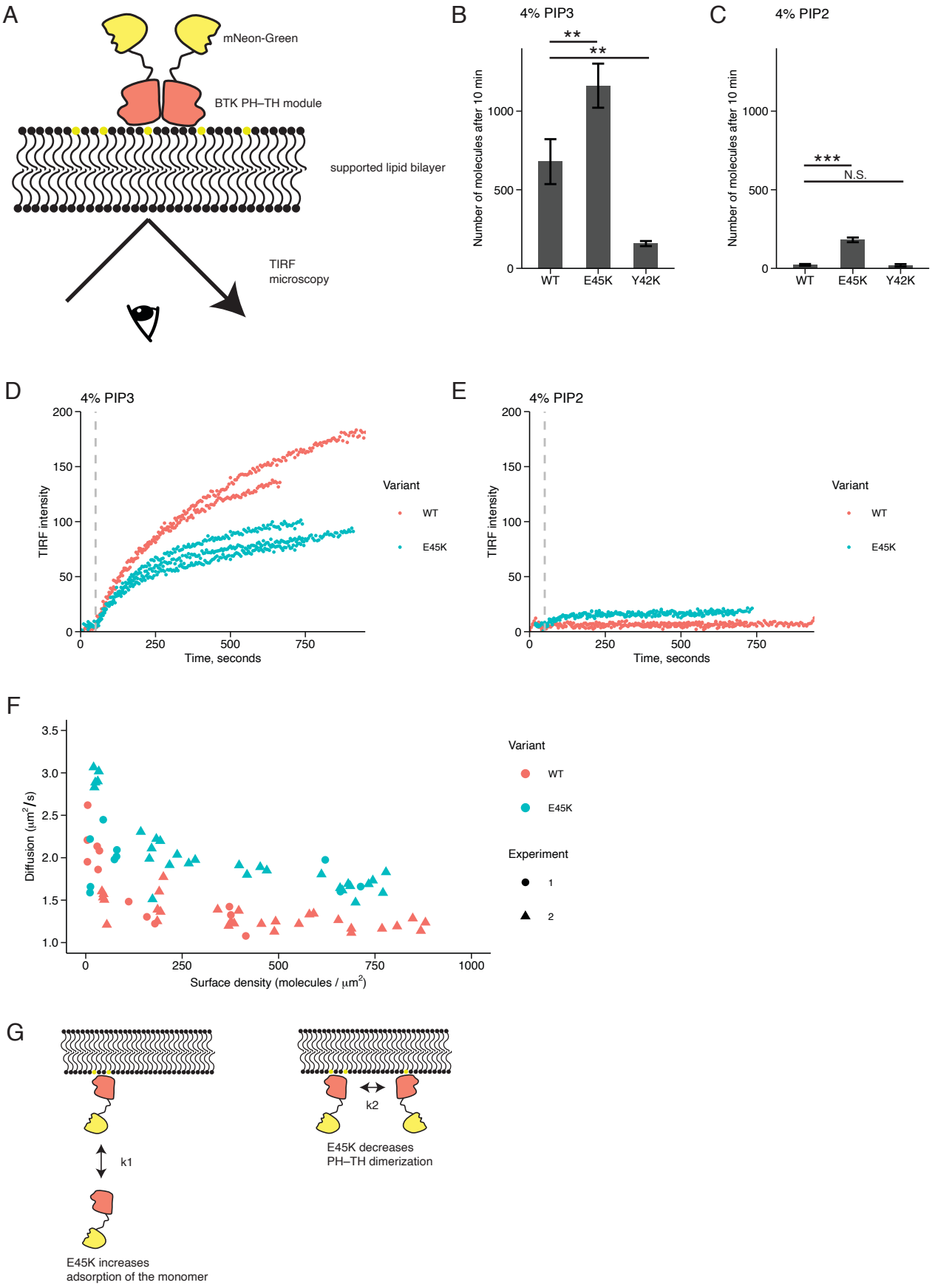
A
mNeon-Green
BTK PH–TH module
supported lipid bilayer
TIRF
microscopy
B
4% PIP3
**
**
Number of molecules after 10 min
1000
500
0
WT
E45K
Y42K
C
4% PIP2
***
N.S.
Number of molecules after 10 min
1000
500
0
WT
E45K
Y42K
D
4% PIP3
TIRF intensity
200
150
100
50
0
0
250
500
750
Time, seconds
Variant
WT
E45K
E
4% PIP2
TIRF intensity
200
150
100
50
0
0
250
500
750
Time, seconds
Variant
WT
E45K
F
Diffusion (μm²/s)
3.5
3.0
2.5
2.0
1.5
1.0
0
250
500
750
1000
Surface density (molecules / μm²)
Variant
WT
E45K
Experiment
1
2
G
k1
E45K increases
adsorption of the monomer
k2
E45K decreases
PH–TH dimerization

Figure S1

A

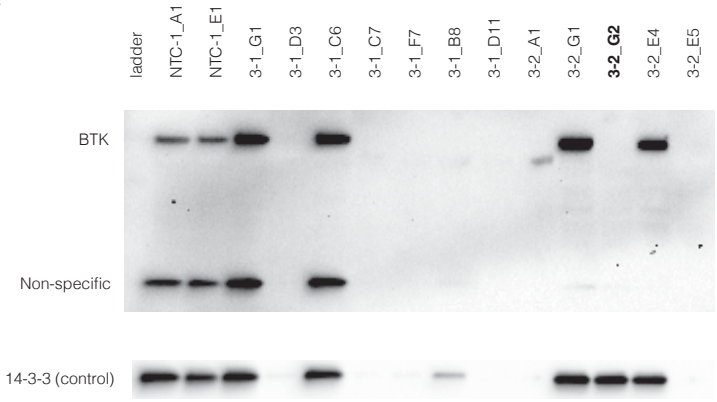

B

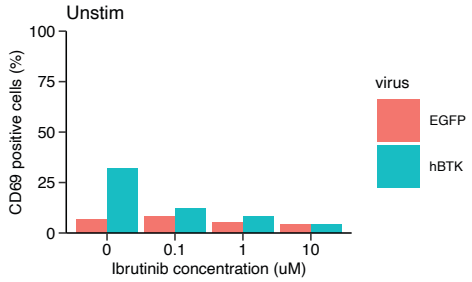

C

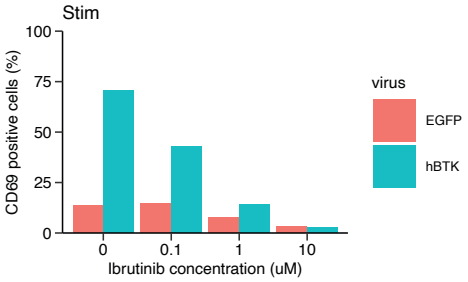

D

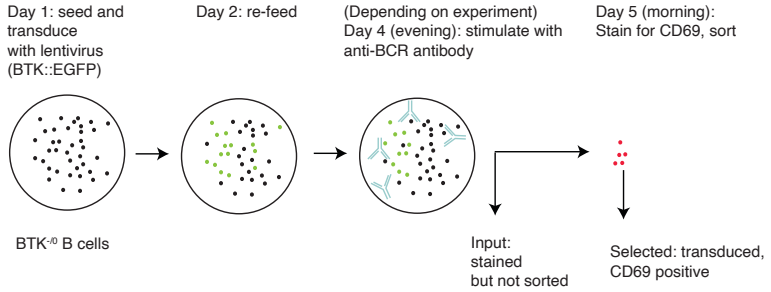

E

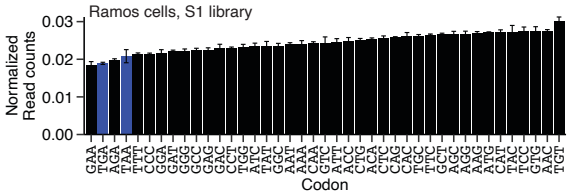

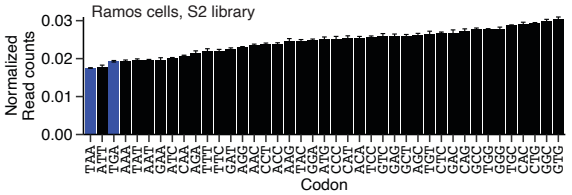

F

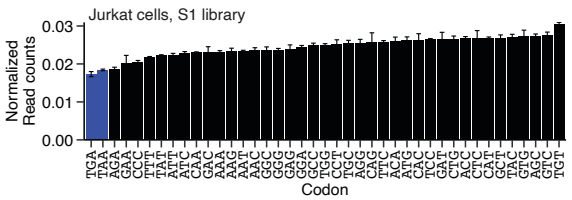

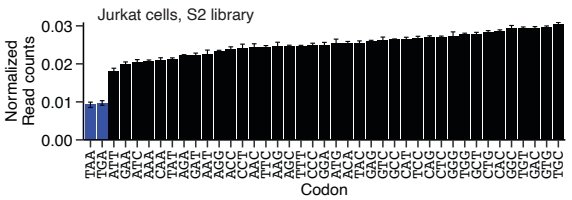

Figure S2

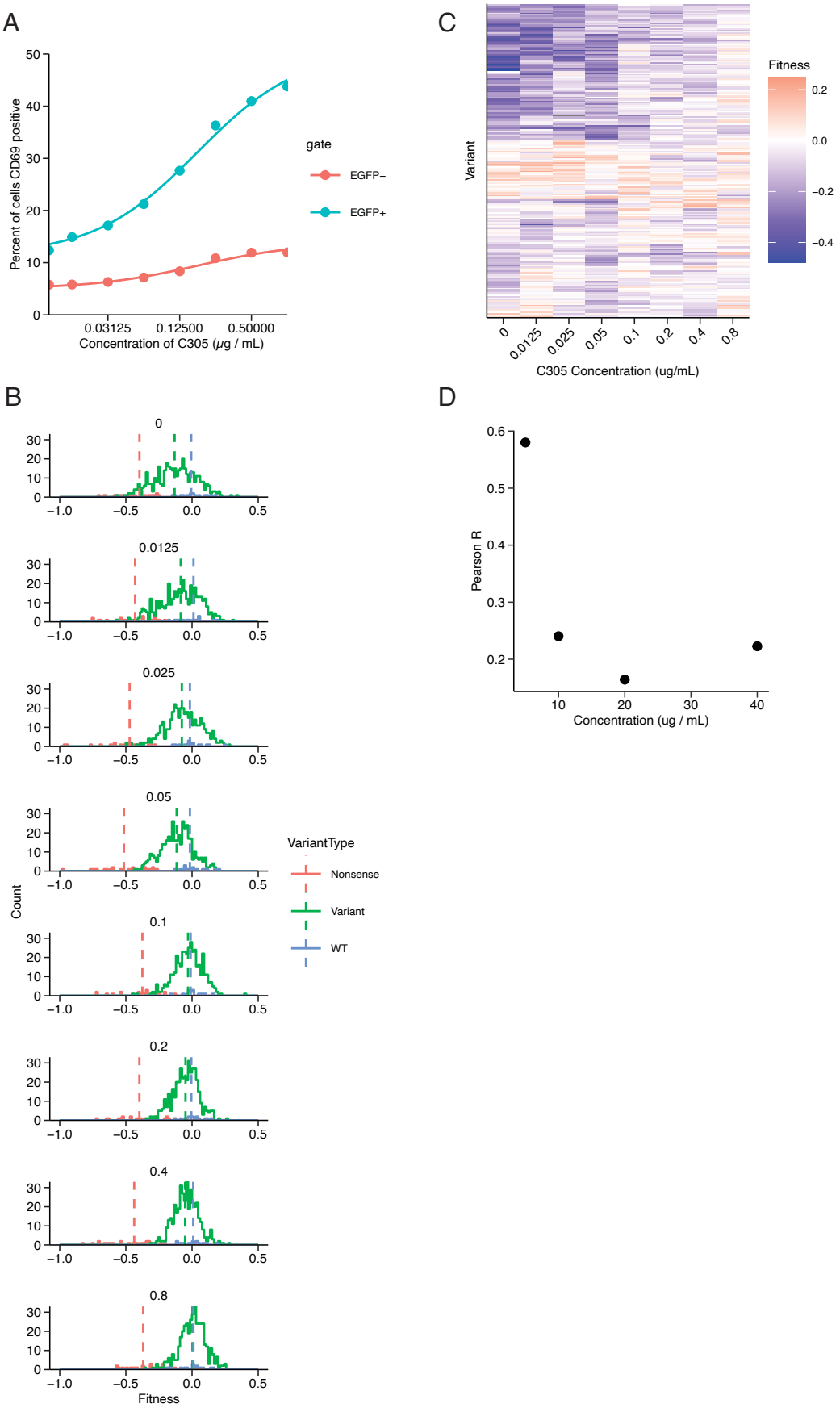
A
Percent of cells CD69 positive
Concentration of C305 (μg / mL)
0.03125
0.12500
0.50000
gate
EGFP−
EGFP+
C
Variant
Fitness
C305 Concentration (ug/mL)
0
0.0125
0.025
0.05
0.1
0.2
0.4
0.8
B
Count
Fitness
VariantType
Nonsense
Variant
WT
D
Pearson R
Concentration (ug / mL)

Figure S3

A

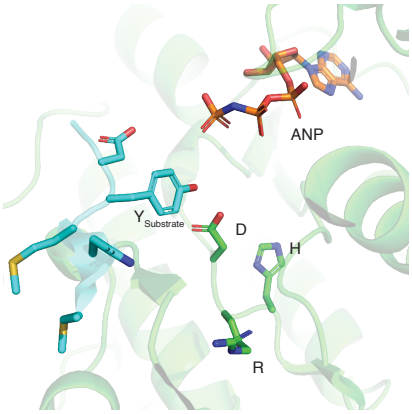
ANP
Y Substrate
D
H
R

B

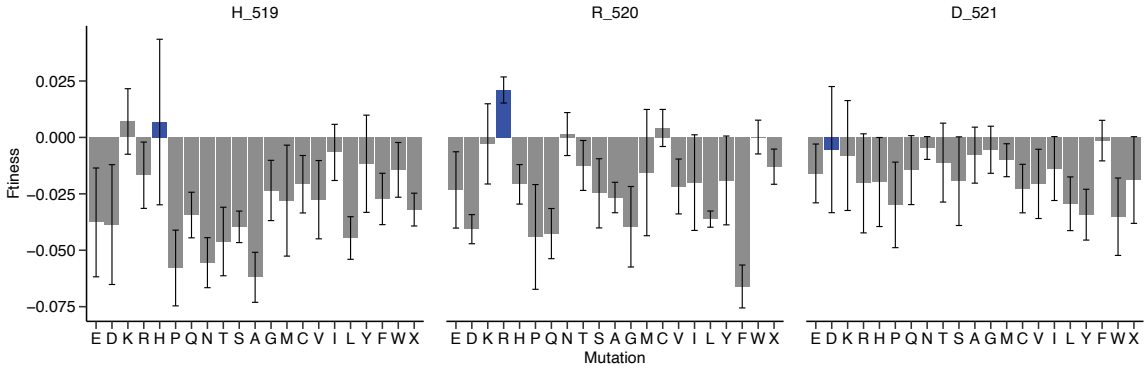
H_519
R_520
D_521
Fitness
0.025
0.000
−0.025
−0.050
−0.075
E D K R H P Q N T S A G M C V I L Y F W X
Mutation

Figure S4

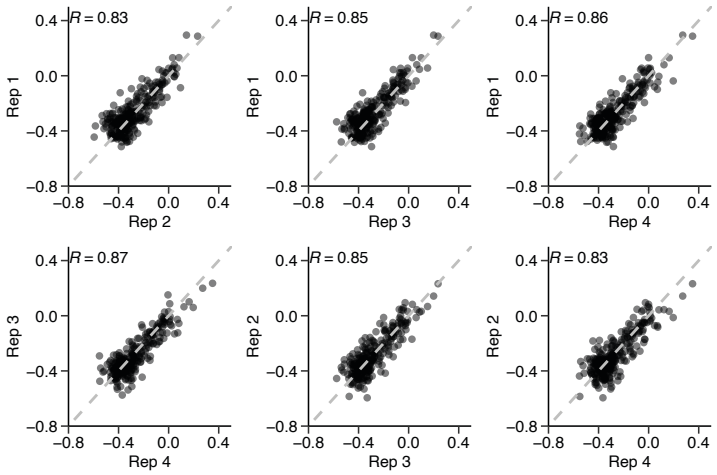
R = 0.83
Rep 1
Rep 2
R = 0.85
Rep 1
Rep 3
R = 0.86
Rep 1
Rep 4
R = 0.87
Rep 3
Rep 4
R = 0.85
Rep 2
Rep 3
R = 0.83
Rep 2
Rep 4
0.4
0.0
−0.4
−0.8

Figure S5

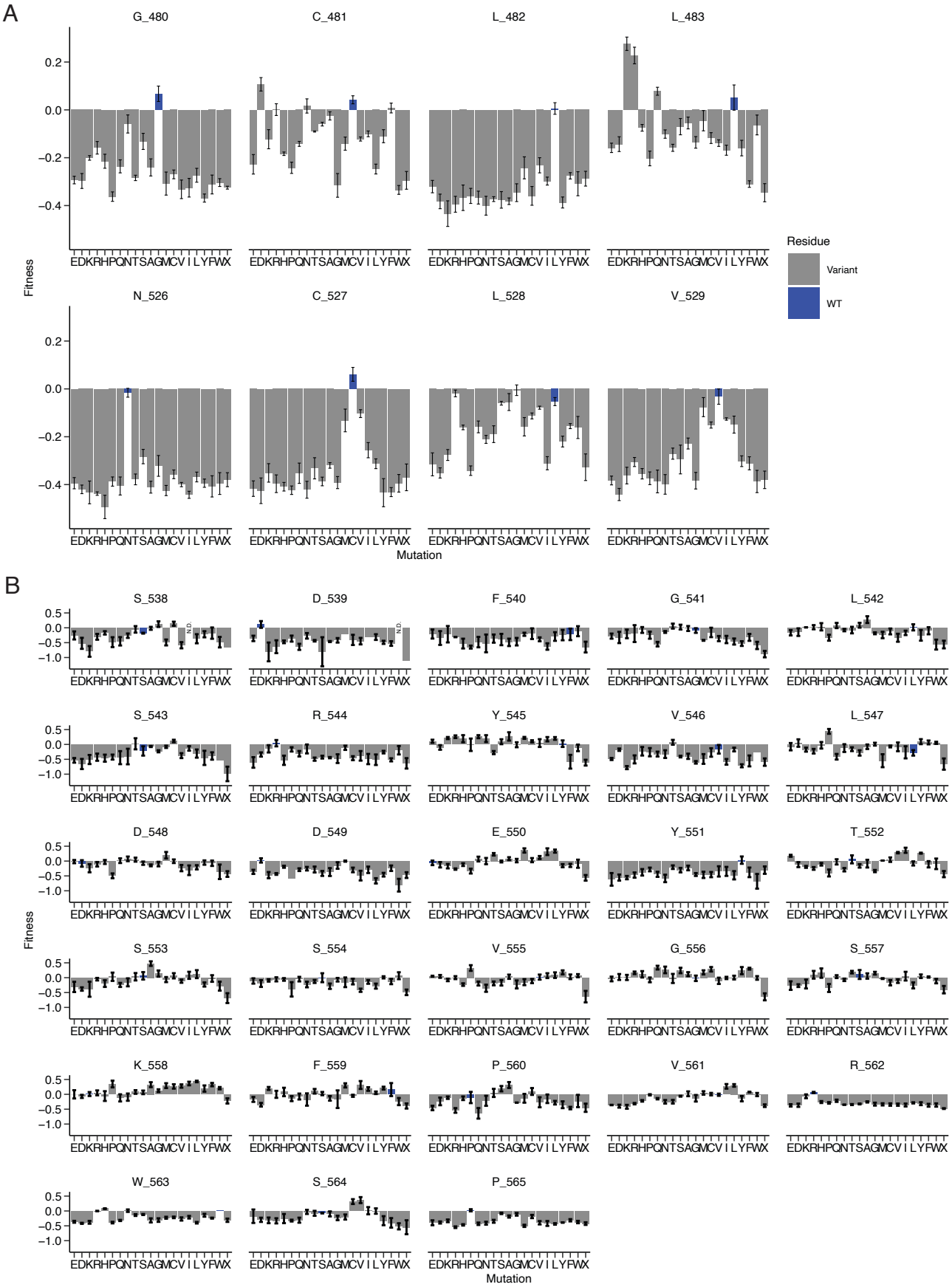
A
G_480
C_481
L_482
L_483
N_526
C_527
L_528
V_529
Fitness
Mutation
Residue
Variant
WT
B
S_538
D_539
F_540
G_541
L_542
S_543
R_544
Y_545
V_546
L_547
D_548
D_549
E_550
Y_551
T_552
S_553
S_554
V_555
G_556
S_557
K_558
F_559
P_560
V_561
R_562
W_563
S_564
P_565
N.D.
EDKRHPQNTSAGMCV I LYFWX

Figure S6

A

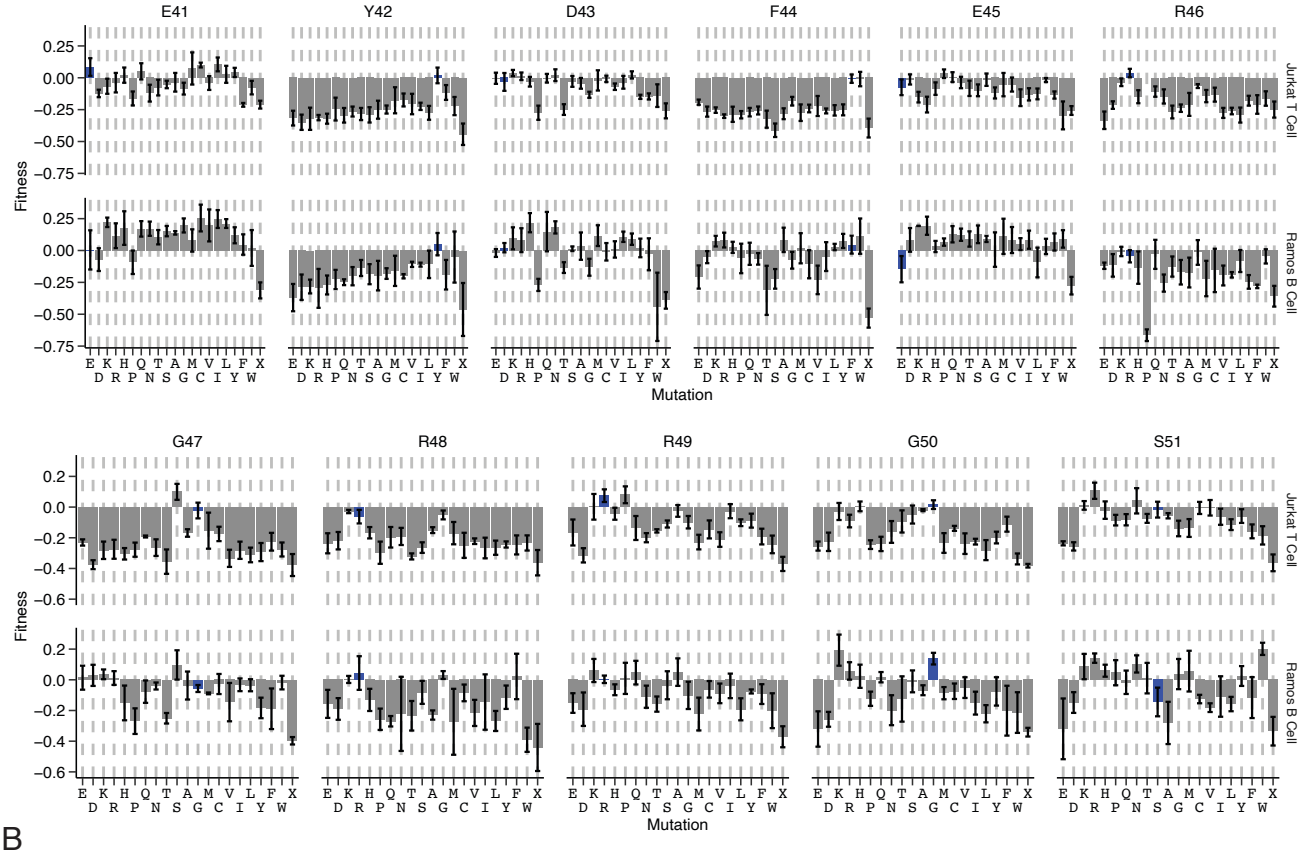
E41
Y42
D43
F44
E45
R46
G47
R48
R49
G50
S51
Jurkat T Cell
Ramos B Cell
Fitness
Mutation
E K H Q T A M V L F X
D R P N S G C I Y W

B

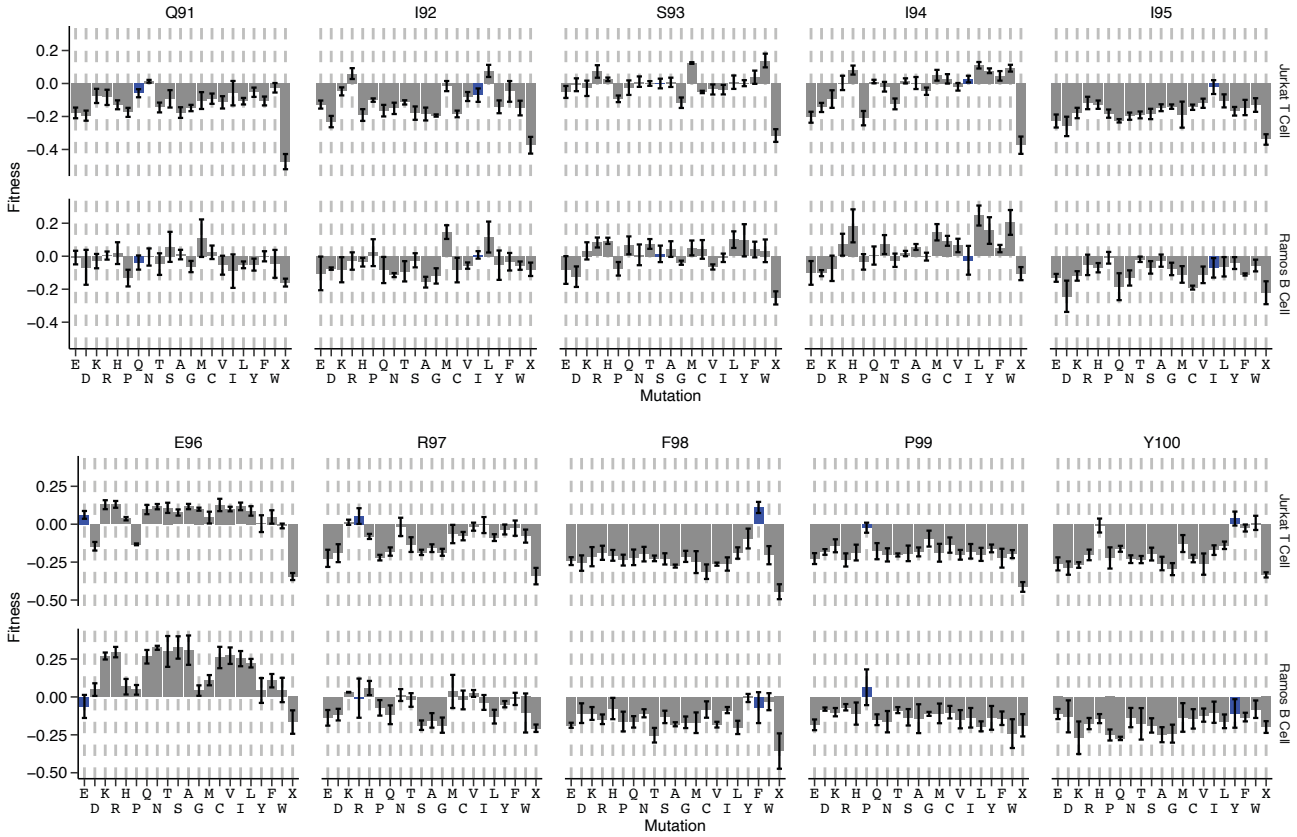
Q91
I92
S93
I94
I95
E96
R97
F98
P99
Y100
Jurkat T Cell
Ramos B Cell
Fitness
Mutation
E K H Q T A M V L F X
D R P N S G C I Y W

Figure S7

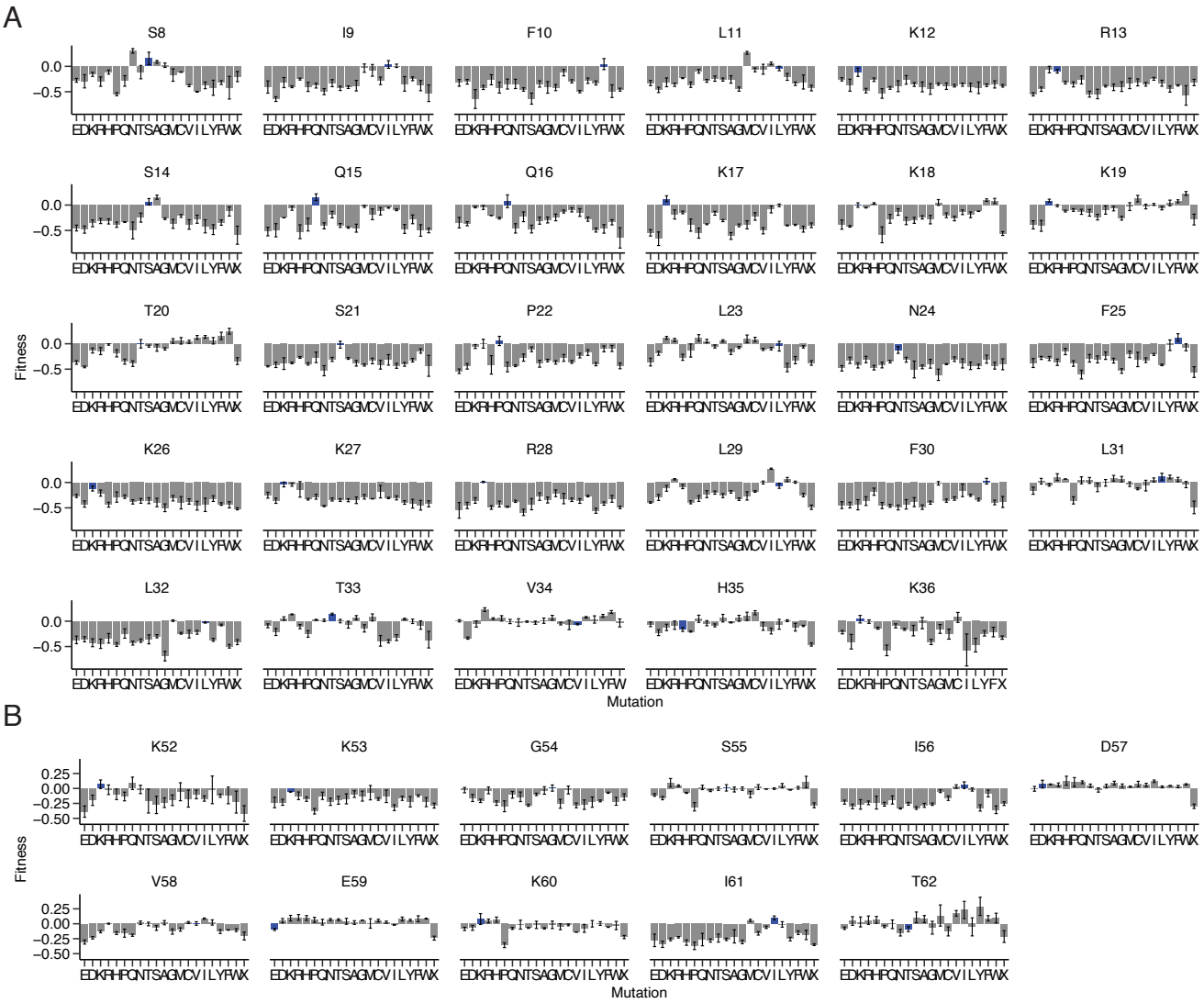
A
S8
I9
F10
L11
K12
R13
S14
Q15
Q16
K17
K18
K19
T20
S21
P22
L23
N24
F25
K26
K27
R28
L29
F30
L31
L32
T33
V34
H35
K36
Fitness
0.0
−0.5
EDKRHPQNTSAGMCVILYFWX
Mutation
B
K52
K53
G54
S55
I56
D57
V58
E59
K60
I61
T62
0.25
0.00
−0.25
−0.50

Figure S8

A

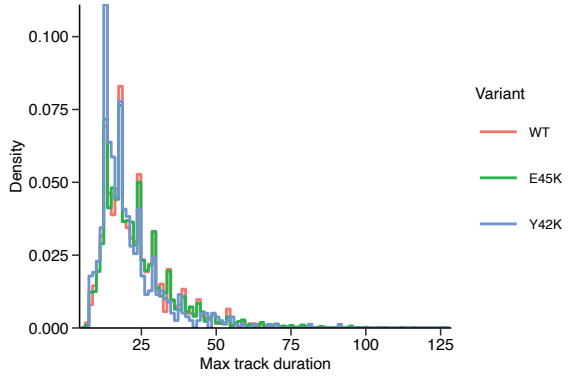

B

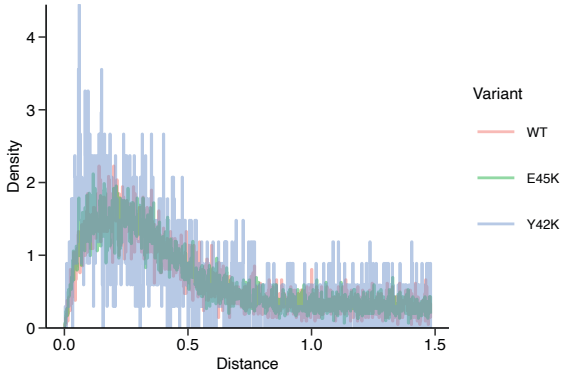

C

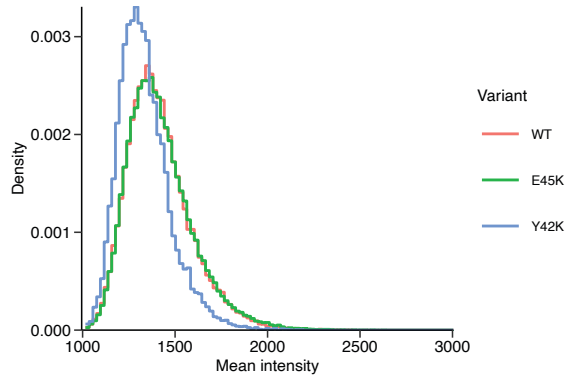

D

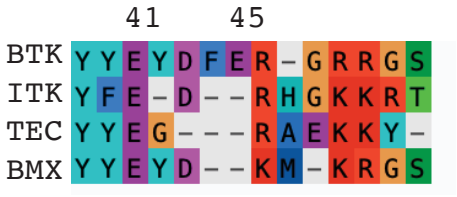

E

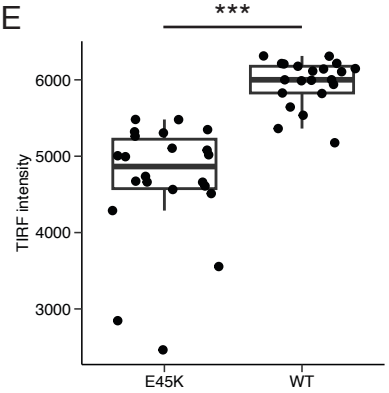

F

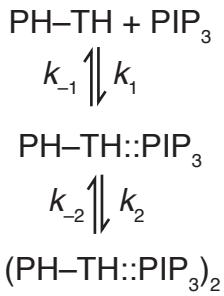
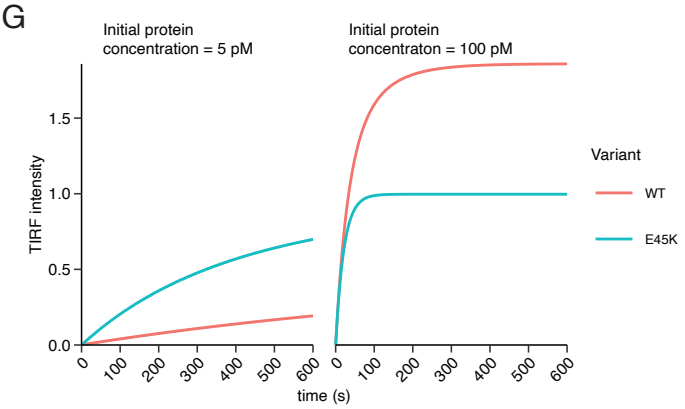
G